AGU PUBLICATIONS

JGR

Journal of Geophysical Research: Space Physics

RESEARCH ARTICLE

10.1002/2016JA022850

Key Points:
- Linear properties of ion Bernstein modes are examined with varying proton-to-electron mass ratio
- Low- and high-frequency harmonic modes respond differently to the change of mass ratio
- Dependence of the low- and high-frequency harmonic modes on the mass ratio is obtained

Supporting Information:
- Supporting Information S1

Correspondence to:
K. Min,
kyungguk.min@jhuapl.edu

Citation:
Min, K., and K. Liu (2016), Ion Bernstein instability dependence on the proton-to-electron mass ratio: Linear dispersion theory, *J. Geophys. Res. Space Physics*, *121*, 6692–6710, doi:10.1002/2016JA022850.

Received 21 APR 2016
Accepted 7 JUL 2016
Accepted article online 13 JUL 2016
Published online 28 JUL 2016

Ion Bernstein instability dependence on the proton-to-electron mass ratio: Linear dispersion theory

Kyungguk Min[1,2] and Kaijun Liu[1]

[1]Department of Physics, Auburn University, Auburn, Alabama, USA, [2]The Johns Hopkins University Applied Physics Laboratory, Laurel, Maryland, USA

Abstract Fast magnetosonic waves, which have as their source ion Bernstein instabilities driven by tenuous ring-like proton velocity distributions, are frequently observed in the inner magnetosphere. One major difficulty in the simulation of these waves is that they are excited in a wide frequency range with discrete harmonic nature and require time-consuming computations. To overcome this difficulty, recent simulation studies assumed a reduced proton-to-electron mass ratio, m_p/m_e, and a reduced light-to-Alfvén speed ratio, c/v_A, to reduce the number of unstable modes and, therefore, computational costs. Although these studies argued that the physics of wave-particle interactions would essentially remain the same, detailed investigation of the effect of this reduced system on the excited waves has not been done. In this study, we investigate how the complex frequency, $\omega = \omega_r + i\gamma$, of the ion Bernstein modes varies with m_p/m_e for a sufficiently large c/v_A (such that $\omega_{pe}^2/\Omega_e^2 \equiv (m_e/m_p)(c/v_A)^2 \gg 1$) using linear dispersion theory assuming two different types of energetic proton velocity distributions, namely, ring and shell. The results show that low- and high-frequency harmonic modes respond differently to the change of m_p/m_e. For the low harmonic modes (i.e., $\omega_r \sim \Omega_p$), both ω_r/Ω_p and γ/Ω_p are roughly independent of m_p/m_e, where Ω_p is the proton cyclotron frequency. For the high harmonic modes (i.e., $\Omega_p \ll \omega_r \lesssim \omega_{\mathrm{lh}}$, where ω_{lh} is the lower hybrid frequency), $\gamma/\omega_{\mathrm{lh}}$ (at fixed $\omega_r/\omega_{\mathrm{lh}}$) stays independent of m_p/m_e when the parallel wave number, $k_\parallel$, is sufficiently large and becomes inversely proportional to $(m_p/m_e)^{1/4}$ when $k_\parallel$ goes to zero. On the other hand, the frequency range of the unstable modes normalized to ω_{lh} remains independent of m_p/m_e, regardless of $k_\parallel$.

1. Introduction

Enhanced magnetic and electric field fluctuation spectra with peaks at frequencies close to the proton cyclotron frequency, Ω_p, and its harmonics up to and beyond the lower hybrid frequency, ω_{lh}, have been observed near the geomagnetic equator of the terrestrial magnetosphere at radial distances between 2 and 8 R_E [*Russell et al.*, 1970; *Perraut et al.*, 1982; *Santolík et al.*, 2002; *Boardsen et al.*, 2016]. The waves propagate nearly perpendicular to the background magnetic field ($\mathbf{B}_0$) [*Boardsen et al.*, 1992; *Santolík et al.*, 2002], are primarily confined within 2–3° of the geomagnetic equator [*Němec et al.*, 2005, 2006], and are mainly observed in the afternoon and premidnight sectors [*Ma et al.*, 2016]. These waves are called fast magnetosonic waves because the wave properties are consistent with the prediction using the cold plasma dispersion relation for fast magnetosonic waves [*Boardsen et al.*, 1992; *Walker et al.*, 2015; *Boardsen et al.*, 2016].

Observations [*Perraut et al.*, 1982; *Boardsen et al.*, 1992; *Meredith et al.*, 2008] and linear theory studies [*Gul'elmi et al.*, 1975; *McClements et al.*, 1994; *Chen et al.*, 2010a] suggest that the waves are driven by energetic protons at energies of tens of keV which have ring-like velocity distributions with $\partial f_p(v_\perp)/\partial v_\perp > 0$, where $f_p(v_\perp)$ is the perpendicular velocity distribution function. Statistical observations show that the ring-like proton velocity distributions mainly appear near dusk [*Meredith et al.*, 2008; *Thomsen et al.*, 2011] due partly to energy-dependent drift of injected ring current ions [*Chen et al.*, 2010a]. With a sufficiently steep positive slope of $f_p(v_\perp)$, kinetic linear dispersion theory in a homogeneous, collisionless, magnetized plasma predicts narrow bands of unstable ion Bernstein modes at $0 \le k_\parallel \ll k_\perp$ and near harmonics of Ω_p [e.g., *Gul'elmi et al.*, 1975; *Perraut et al.*, 1982; *Boardsen et al.*, 1992; *Horne et al.*, 2000], where k denotes the wave number and the subscripts denote the directions parallel and perpendicular to $\mathbf{B}_0$. *Perraut et al.* [1982] considered a two-component proton velocity distribution consisting of a cold proton background and a cold proton ring

for linear dispersion analyses. With a sufficiently tenuous cold proton ring component consistent with plasma conditions found in the inner magnetosphere, they showed that the proton ring-driven instabilities are excited near the crossings between the fast magnetosonic mode dispersion relation and the multiple dispersion branches of the various ion Bernstein modes. Therefore, the fast magnetosonic waves have as their source the ion Bernstein instability and exhibit proton cyclotron harmonic structure.

There are also cases where the narrow bands are observed at off-harmonic frequencies, often with frequency spacings substantially deviating from integer multiples of Ω_p, or the frequency spectrum does not exhibit any discrete bands at all, but broadband structures; examples of these cases have been recently reported by *Posch et al.* [2015]. One explanation for the odd harmonicity of fast magnetosonic waves is that the waves can propagate across the field lines [*Kasahara et al.*, 1994; *Horne et al.*, 2000; *Chen and Thorne*, 2012; *Xiao et al.*, 2012, 2015]. Although they were excited at the harmonics of Ω_p in the source region, the wave frequencies normalized to the local Ω_p vary, as the waves propagate radially. Observationally, *Němec et al.* [2013] confirmed the azimuthal as well as radial components of the wave normal vector with directions dependent upon the location relative to the plasmapause. *Hrbáčková et al.* [2015] showed an azimuthal asymmetry of the occurrence rate of the waves outside of the plasmasphere but a relatively uniform distribution inside, favoring the hypothesis that fast magnetosonic waves are generated in the afternoon sector of the plasmapause region and propagate both inward and outward. Another explanation simply invokes linear theory in local plasmas. *Horne et al.* [2000] and *Chen et al.* [2016] showed that the growth rates of the ion Bernstein instabilities can be continuous. *Min and Liu* [2015a, 2016a] showed that the growth rates do not necessarily peak at the exact harmonics of Ω_p when a more realistic partial shell or isotropic shell proton velocity distribution is considered. There is also the possibility that nonlinear wave-wave interactions may contribute as *Perraut et al.* [1982] suggested.

One major difficulty in studying the fast magnetosonic waves is that the waves are excited in a wide frequency range (roughly between Ω_p and $\omega_{\rm lh}$), which means that both ion and electron kinetics should be considered in linear analyses and kinetic simulations. In particle-in-cell (PIC) simulations, this translates to a large number of simulation cells (thus more computational resources) needed to resolve both large- and small-scale Bernstein modes. In terms of linear theory analyses, identifying multiple Bernstein dispersion surfaces becomes tedious and requires substantial computing time because of the increasing number of harmonic sums needed for the convergence of the kinetic dispersion relation and the increasing computational cost of evaluating the transcendental Bessel functions at large harmonic numbers. To overcome these challenges, recent studies [*Liu et al.*, 2011; *Min and Liu*, 2015a, 2015b, 2016b, *Min et al.*, 2016; *Min and Liu*, 2016a] resorted to a reduced system where the proton-to-electron mass ratio, m_p/m_e, and the light-to-Alfvén speed ratio, c/v_A, are substantially reduced. Although the reduced system has a fewer number of unstable modes because the number of harmonics excited is dependent upon $\omega_{\rm lh}$ which can be expressed as $\omega_{\rm lh} = \Omega_p/\sqrt{v_A^2/c^2 + m_e/m_p}$ (where m_e/m_p is the electron to proton mass ratio), they argued that the waves excited still exhibit the general ion Bernstein mode dispersion properties. Nevertheless, more quantitative justification of employing such a reduced system is needed, and the present paper is aimed at delivering this goal from a linear theory point of view.

Better understanding the scaling properties of the Bernstein instabilities with m_p/m_e is advantageous in many aspects because this parameter (combined with c/v_A) determines $\omega_{\rm lh}$ and thus the number of the discrete harmonic modes excited. Moreover, *Sun et al.* [2016a, 2016b] showed that it is also related to the overall growth rates of these wave modes. If the scaling is well defined, one can wisely choose m_p/m_e to reduce computational costs while keeping the necessary physics and then properly scale the results back to the realistic situation. *Sun et al.* [2016a, 2016b] recently studied the dependence of the instability growth rate on m_p/m_e and c/v_A but only considered exact perpendicular propagation with $k_\parallel = 0$. Using linear theory with a cold (delta function) ring and 1-D PIC simulations, they showed that the growth rate increases with increasing m_p/m_e and c/v_A and that the discrete unstable mode can merge into a continuum when the growth rate becomes sufficiently large. The present study is focused on the dependence of the ion Bernstein modes for $k_\parallel/k_\perp \geq 0$ on m_p/m_e for sufficiently large c/v_A consistent with inner magnetospheric conditions.

The paper is organized as follows: section 2 provides an overview of the full linear theory solutions and section 3 is focused on the detailed analyses. Section 4 summarizes and discusses the results. Same as our previous studies, we denote the jth species plasma frequency as $\omega_{pj} \equiv \sqrt{4\pi n_j e^2/m_j}$, the jth species cyclotron frequency as $\Omega_j \equiv e_j B_0/m_j c$ (with sign retained), and the jth component beta as $\beta_j \equiv 8\pi n_j T_j/B_0^2$. Additionally, we define $\tilde{\beta}_j \equiv 8\pi n_0 T_j/B_0^2$ following *Gary et al.* [2010]. The Alfvén speed is $v_A \equiv B_0/\sqrt{4\pi n_0 m_p}$ and the proton

inertial length is $\lambda_p \equiv \sqrt{m_p c^2/4\pi n_0 e^2}$. Here n_0 is equal to the unperturbed electron density n_e. We assume $\mathbf{B}_0 = B_0\hat{\mathbf{z}}$, real wave number $\mathbf{k} = k_\perp\hat{\mathbf{x}} + k_\parallel\hat{\mathbf{z}}$ (with $\hat{\mathbf{x}} = \hat{\mathbf{y}} \times \hat{\mathbf{z}}$) and complex wave frequency $\omega = \omega_r + i\gamma$ with $\gamma > 0$ indicating a growing mode.

2. Overview

We first present a full linear theory picture of the ion Bernstein instabilities driven by two types of ring-like proton velocity distributions for four different proton-to-electron mass ratios—m_p/m_e = 100, 400, 900, and 1836—and outline the key features that will be addressed in the following section. For all analyses presented, we assume a homogeneous, magnetized, and collisionless plasma consisting of core electrons and protons represented by a single Maxwellian distribution with a small temperature and tenuous but energetic protons which drive the instability of interest. It should be noted that the "shape" of the velocity distributions, particularly, those with a high-energy tail, are critical for instability analysis for both ion- [e.g., *Mace et al.*, 2011; *Sugiyama et al.*, 2015; *Shaaban et al.*, 2016] and electron-scale instabilities [e.g., *Mace*, 2004; *Mace and Hellberg*, 2009; *Qureshi et al.*, 2014]. For example, energetic particles of the magnetospheric plasma often have a high-energy tail so a kappa-type distribution may be a better choice [e.g., *Viñas et al.*, 2005; *Xiao et al.*, 2007, 2008]. In this study, however, we mainly focus on gaining physical insights into the m_p/m_e dependence of the Bernstein instability by choosing a single Maxwellian for the core components.

As in *Min and Liu* [2016a] (referred to as paper 1 hereinafter), we use two different model proton distributions that contain one ring and one shell, respectively. The first model distribution consists of a relatively dense, relatively cold core Maxwellian proton component (f_c), and a relatively tenuous, warm ring proton component (f_r) which is defined as

$$\begin{aligned} f_r &\equiv \frac{1}{\pi^{3/2}\theta_r^3 C_r} e^{-v_\parallel^2/\theta_r^2} e^{-(v_\perp - v_r)^2/\theta_r^2}, \\ C_r &\equiv e^{-v_r^2/\theta_r^2} + \sqrt{\pi}\left(\frac{v_r}{\theta_r}\right)\mathrm{erfc}\left(-\frac{v_r}{\theta_r}\right), \end{aligned} \tag{1}$$

where θ_r and v_r denote the ring thermal speed and the ring speed, respectively, and erfc(x) is the complementary error function. This model will be referred to as "ring model." For the second model, the ring component is replaced with an isotropic shell (f_s) velocity distribution which is defined as

$$\begin{aligned} f_s &\equiv \frac{1}{\pi^{3/2}\theta_s^3 C_s} e^{-(v - v_s)^2/\theta_s^2}, \\ C_s &\equiv \frac{2}{\sqrt{\pi}}\left[\frac{v_s}{\theta_s} e^{-v_s^2/\theta_s^2} + \sqrt{\pi}\left(\frac{1}{2} + \frac{v_s^2}{\theta_s^2}\right)\mathrm{erfc}\left(-\frac{v_s}{\theta_s}\right)\right], \end{aligned} \tag{2}$$

where θ_s and v_s denote the shell thermal speed and the shell speed, respectively, and $v \equiv \sqrt{v_\perp^2 + v_\parallel^2}$. So this model will be referred to as "shell model."

Similarly, we choose $\tilde{\beta}_c = 0.002$, $\theta_r^2/v_A^2 = \theta_s^2/v_A^2 = 0.2$, and $n_r/n_0 = n_s/n_0 = 0.01$ and assume that electrons are represented by a single Maxwellian distribution with $\beta_e = \tilde{\beta}_c$. Unlike paper 1, however, we choose as a nominal value a sufficiently large light-to-Alfvén speed ratio of $c/v_A = 400$ similar to the values found in the inner magnetosphere. Using these parameters and proton model distributions, a full kinetic linear dispersion relation solver [*Min and Liu*, 2015a] is used to calculate the properties of ion Bernstein instabilities (readers are referred to *Min et al.* [2016] for details of handling the shell velocity distribution of equation (2) in the linear analyses).

Figures 1a and 1b display the full linear theory solutions for the ring model with $v_r/v_A = 2$ and 1.2 in $k_\parallel$-$k_\perp$ space, respectively. Here $k_\parallel$ and $k_\perp$ are normalized to λ_p^{-1}, and the maximum $k_\perp$ value on the horizontal axis is chosen to be $8\lambda_e^{-1}$ (more discussion in the next paragraph), where $\lambda_e \equiv c/\omega_{pe} = \sqrt{m_e/m_p}\lambda_p$ denotes the electron inertial length. With a similar format, Figure 2 displays the full linear theory solutions for the shell model with $v_s/v_A = 2$.

Three features are highlighted as follows. First, the extent of unstable modes in $k_\parallel$ space appears to be well regulated by λ_p irrespective of m_p/m_e. This is especially apparent for the shell model where the alternating growth and damping patterns in $k_\parallel\lambda_p$ space are remarkably consistent regardless of m_p/m_e. For the ring model case, however, the unstable modes near $k_\perp = 8\lambda_e^{-1}$ extend slightly to larger $k_\parallel$ for larger m_p/m_e. These

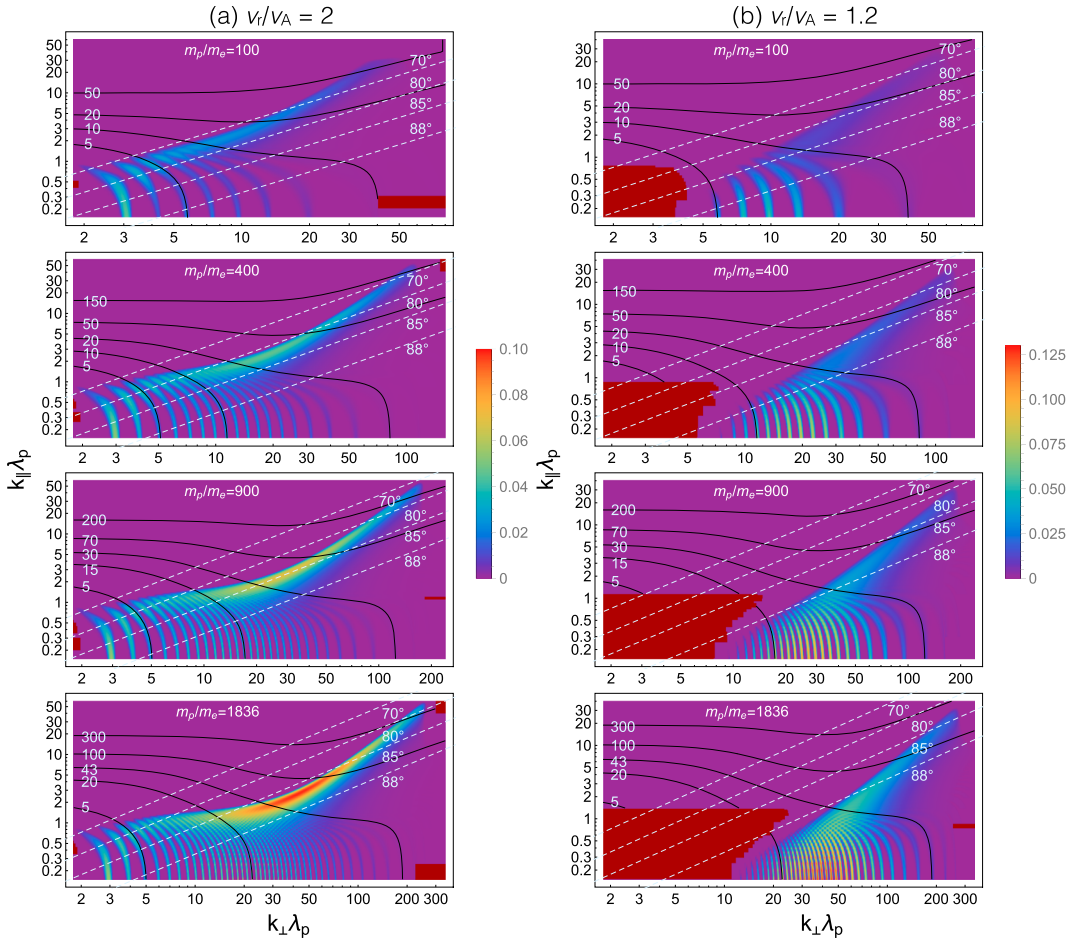

Figure 1. Full linear theory solutions for the ring model with (a) $v_r/v_A = 2$ and (b) $v_r/v_A = 1.2$ in $k_\parallel$-$k_\perp$ space for m_p/m_e = 100, 400, 900, and 1836. The minimum and maximum $k_\perp$ values are $1.8\lambda_p^{-1}$ and $8\lambda_e^{-1}$, respectively. The color intensity represents the growth rates (only the growing modes) whose values normalized to Ω_p are denoted by the color bars (same scale). The solid contours represent the real frequencies normalized to Ω_p, and the four dashed lines mark constant wave normal angles denoted by the labels. The dark red patches are where the dispersion solver failed, and thus, no solutions were available.

complex growth rate patterns have been investigated in paper 1; they are primarily determined by the structure of the gyroaveraged ring-like velocity distribution and the proton cyclotron resonance condition. Since the distribution function used is independent of m_p/m_e and the resonance condition, $v_{res} = (\omega - j\Omega_p)/k_\parallel$, is governed by the proton cyclotron frequency, it is not surprising to see that the patterns are well defined in terms of $k_\parallel\lambda_p$ (rather than $k_\parallel\lambda_e$) regardless of m_p/m_e. Second, the upper $k_\perp$ bound of the unstable modes appears to be well defined in terms of λ_e rather than λ_p, whereas the lower $k_\perp$ bound is well defined in terms of λ_p. Therefore, although the absolute growth rate magnitudes are different, the unstable modes appear to be well contained within the range of $\lambda_p^{-1} \lesssim k_\perp \lesssim \lambda_e^{-1}$. Third, the number of unstable modes and the overall growth rates apparently increase with increasing m_p/m_e. The former characteristic can be easily understood because ω_{lh}, which increases with increasing m_p/m_e, is closely related to the upper frequency bound of the unstable modes [e.g., *Boardsen et al.*, 2016]. The latter characteristic will be further explored in section 3.

3. Analyses

Since the first point can be explained from the results of paper 1, we here focus on investigating the remaining two features. The analyses in this section are done by comparing the real frequencies and growth rates of the ion Bernstein modes for the four different m_p/m_e values at fixed $k_\parallel$. To facilitate the analyses, we define two scales: proton kinetic scale where $\omega_r \sim \Omega_p$ and $k\lambda_p \sim 1$ and electron kinetic scale where $\Omega_p \ll \omega_r \lesssim \omega_{lh}$

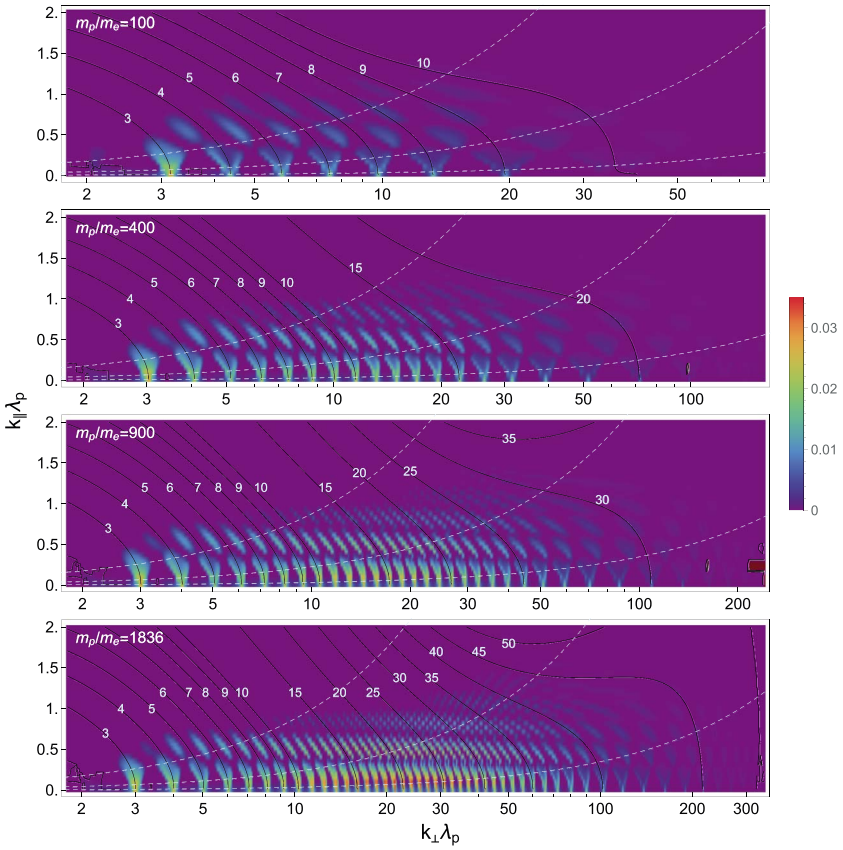

Figure 2. Full linear theory solutions for the shell model with $v_s/v_A = 2$ for $m_p/m_e = 100$, 400, 900, and 1836. The format is similar to Figure 1. The minimum and maximum $k_\perp$ values are $1.8\lambda_p^{-1}$ and $8\lambda_e^{-1}$, respectively, and the vertical and horizontal axes are in linear and logarithmic scales, respectively. The irregular contours near $\omega_r/\Omega_p = 2$ and large $k_\perp$ are an artifact caused by multiple dispersion curves and gaps between the neighboring curves.

and $k\lambda_e \sim 1$. Approximate growth rate formulae corresponding to these two different scales are derived in Appendix A and will be employed to help interpret the full linear theory results.

3.1. Dependence of Dispersion Relation on m_p/m_e

Figure 3 plots ω_r versus k for the four different values of m_p/m_e. Due to the dominance of the cold, core proton and electron components, the full linear theory dispersion relations for the unstable modes are close to the cold plasma dispersion relations for the fast magnetosonic waves (not shown). On the other hand, the general electromagnetic ion Bernstein modes can have multiple dispersion branches (due to ion kinetic effect), which are indicated by the nearly horizontal portions of the solid lines in Figures 3a and 3d (corresponding to $k_\parallel = 0$) and are not present in the cold plasma dispersion relation [e.g., *Curtis and Wu*, 1979, Figure 2]. As $k_\parallel$ becomes sufficiently large (or wave normal angle is sufficiently away from 90°), the dispersion solver is able to find the solutions continuously as shown in the figure for the $k_\parallel > 0$ cases. There still should be multiple ion Bernstein dispersion curves approaching the proton cyclotron harmonic frequencies as for the $k_\parallel = 0$ case, but we did not attempt to find them since the strongly growing modes appear only near the intersections of the cold plasma dispersion curves for the fast magnetosonic waves and the multiple ion Bernstein dispersion curves when the cold background dominates [e.g., *Min and Liu*, 2015b].

Note the different normalizations chosen for Figures 3a–3f. When normalized to the proton scale as shown in Figures 3a–3c, for all $k_\parallel$ values chosen, the curves essentially coincide with each other in the proton scale and asymptote to or even cross ω_{lh} as $k\lambda_e$ goes above 1. The opposite situation is evident when normalized to the electron scale as shown in Figures 3d–3f. It is not surprising to see such a picture because at low-frequency limit, electron kinetic effect is not expected to be important, and the phase speed should be close to v_A (with sufficiently small plasma beta), whereas at high-frequency limit protons may be treated as massive particles (but keeping their kinetic effect). This picture is also confirmed by the properly approximated

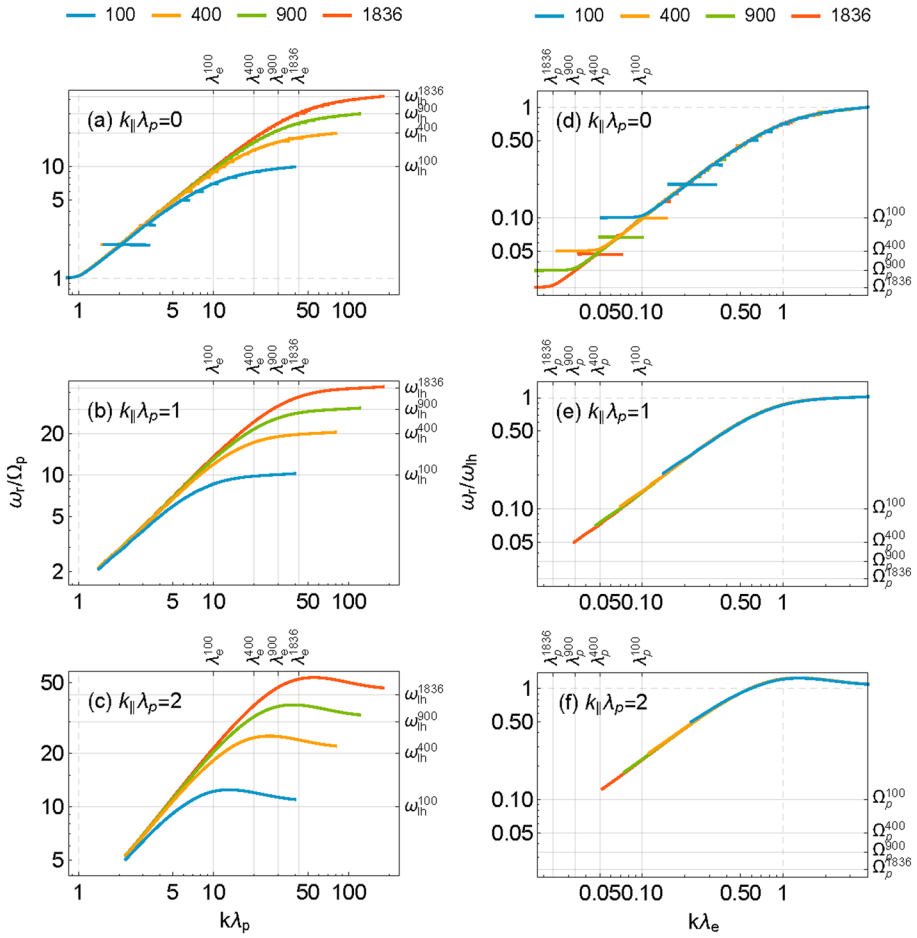

Figure 3. Full linear theory dispersion relations at, from the top, $k_\parallel\lambda_p = 0$, 1 and 2, respectively. (a–c) The real frequencies and the wave numbers are normalized to the proton cyclotron frequency and inverse of the proton inertial length, respectively. The vertical lines, which are labeled as λ_e with the superscripts corresponding to different m_p/m_e, mark the locations of $k\lambda_e = 1$. (d–f) The real frequencies and the wave numbers are normalized to the lower hybrid frequency and inverse of the electron inertial length, respectively. The vertical lines, which are labeled as λ_p with the superscripts corresponding to different m_p/m_e, mark the locations of $k\lambda_p = 1$.

cold plasma dispersion relations for the fast magnetosonic waves given by equations (A25) and (A31) in the electron and proton scales, respectively, which clearly show independence of m_p/m_e (after the corresponding normalization and for fixed $k_\parallel\lambda_p$).

3.2. Dependence of Linear Growth Rate on m_p/m_e

Figure 4 displays the comparison of the growth rates driven by the ring model with $v_r/v_A = 2$ (same as Figure 1) at $k_\parallel\lambda_p \approx 0$, 0.5, 1, 2, and 10 from top to bottom, respectively. Only the local maximum growth rates of the individual harmonic modes, which outline the growth rate envelope, are plotted for the cases with $k_\parallel\lambda_p \le 1$ because of the distinct harmonic peaks. For the $k_\parallel\lambda_p = 2$ and 10 cases, however, the growth rate as a continuous function of frequency is shown and can have two values at a given frequency close to ω_{lh} (see Figure 1). Both the growth rates and real frequencies are normalized to Ω_p in Figure 4 (left column), but to ω_{lh} in Figure 4 (right column).

When normalized to the proton scale in Figure 4 (left column), the maximum growth rates of the first few ($\omega_r/\Omega_p \le 5$) unstable modes remain nearly unchanged for all but the $m_p/m_e = 100$ case. For $m_p/m_e = 100$, they exhibit some deviation from the rest but still appear to have a similar trend. When normalized to the electron scale in Figure 4 (right column), the growth rate envelopes for all but the $m_p/m_e = 100$ case are aligned well in ω_r/ω_{lh} space, except for the first few unstable modes that are organized better when normalized to the proton scale in Figure 4 (left column). Interestingly, γ/ω_{lh} at fixed ω_r/ω_{lh} differs substantially at $k_\parallel\lambda_p \approx 0$ but gradually converges starting from large ω_r/ω_{lh} as $k_\parallel$ increases. The $m_p/m_e = 100$ case exhibits a similar trend

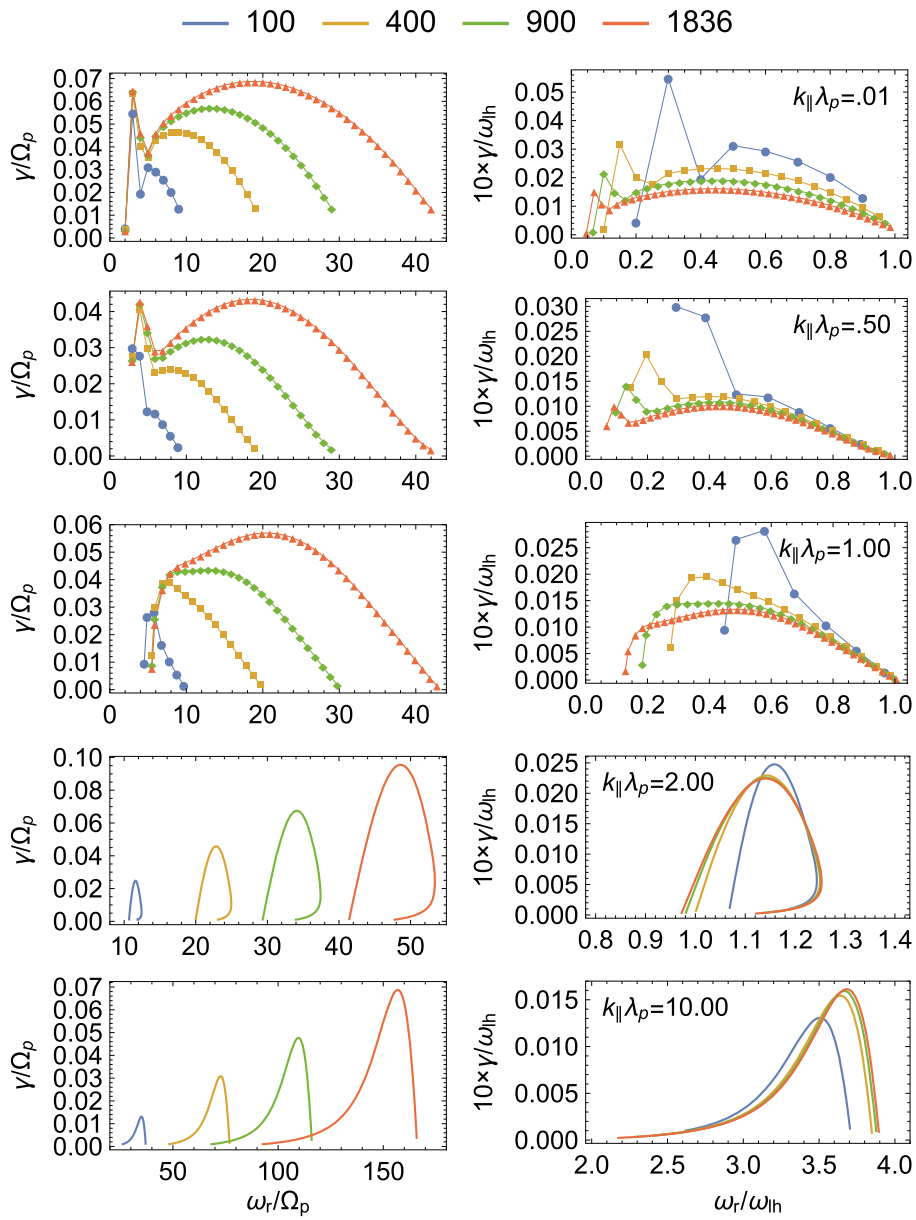

Figure 4. Comparison of the linear growth rates driven by the ring model with $v_r/v_A = 2$ versus the real frequencies for the four different values of m_p/m_e denoted by the line colors (constant $k_\parallel$ slices from Figure 1). From the top, four slices at $k_\parallel \lambda_p = 0.01$, 0.5, 1, 2, and 10 are shown, respectively. Except for the $k_\parallel \lambda_p = 2$ and 10 slices, only the local growth rate maxima of the individual harmonic modes are shown with the symbols (the line segments simply connect them). Both the growth rates and the real frequencies are normalized to the proton cyclotron frequency, Ω_p, in the left column and to the lower hybrid frequency, ω_{lh}, in the right column.

at small $k_\parallel$ but as $k_\parallel$ increases beyond $\sim 2\lambda_p^{-1}$, the unstable modes appear at lower values of ω_r/ω_{lh}, and their γ/ω_{lh} becomes smaller compared to the cases with larger m_p/m_e.

Figure 5 displays the comparison for the ring model with $v_r/v_A = 1.2$. The main difference in this case (compared to Figure 4) is that the lower harmonic modes in the proton scale are now suppressed due to the reduced ring speed. As a result, the consistency of the growth rate envelopes and the convergence of γ/ω_{lh} in the electron scale as described above are more pronounced. Similarly, Figure 6 displays the comparison for the shell model with $v_s/v_A = 2$ (same as Figure 2). Although different $k_\parallel$ slices are shown due to the different growth rate patterns compared to the ring model cases, there exists a consistent trend in both the proton and electron scales with the ring model case with $v_r/v_A = 2$.

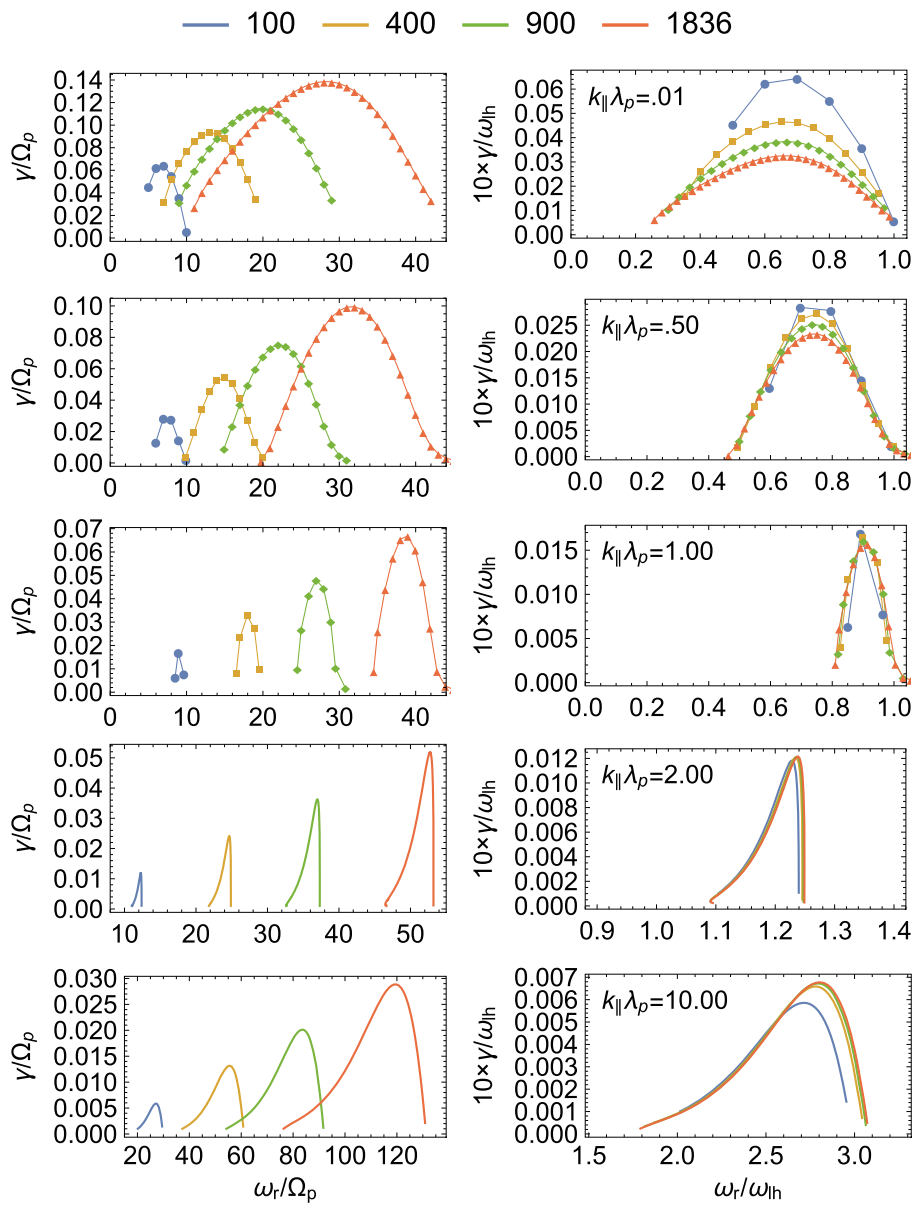

Figure 5. Comparison of the linear growth rates driven by the ring model with $v_r/v_A = 1.2$. The format is the same as Figure 4.

From these comparisons, we highlight two features: (1) the maximum γ/Ω_p at the first few harmonics appear to be independent of m_p/m_e and (2) the maximum γ/ω_{lh} at the higher harmonics (i.e., $\omega_r/\Omega_p \gg 1$) decreases with increasing m_p/m_e for $k_\parallel \approx 0$ but becomes independent of m_p/m_e when $k_\parallel$ increases.

To explain the first feature, we resort to equation (A48), the approximate growth rate formula valid for $k_\parallel = 0$ and for the proton scale. Noting that the argument of the Bessel function, $J_j(x)$, is $x \equiv k_\perp v_\perp/\Omega_p$, the dispersion relation is $\omega_r/k \approx v_A$ and that the velocity distribution function is independent of m_p/m_e, it is apparent that γ/Ω_p is also independent of m_p/m_e. The same argument can be applied to the $k_\parallel \neq 0$ case using equation (A34), although it contains a few extra terms. It should be noted that the $m_p/m_e = 100$ case does not seem to follow this rule as well as the other cases (see Figures 4 (left column) and 6 (left column)). This is because that the smaller the m_p/m_e, the less the number of proton cyclotron harmonic modes for which electron kinetic effect becomes less important. Besides, the dispersion relation for the $m_p/m_e = 100$ case shows the earliest departure from $\omega_r/k = v_A$ at $\omega_r/\Omega_p \approx 3$ compared to the other cases (Figure 3).

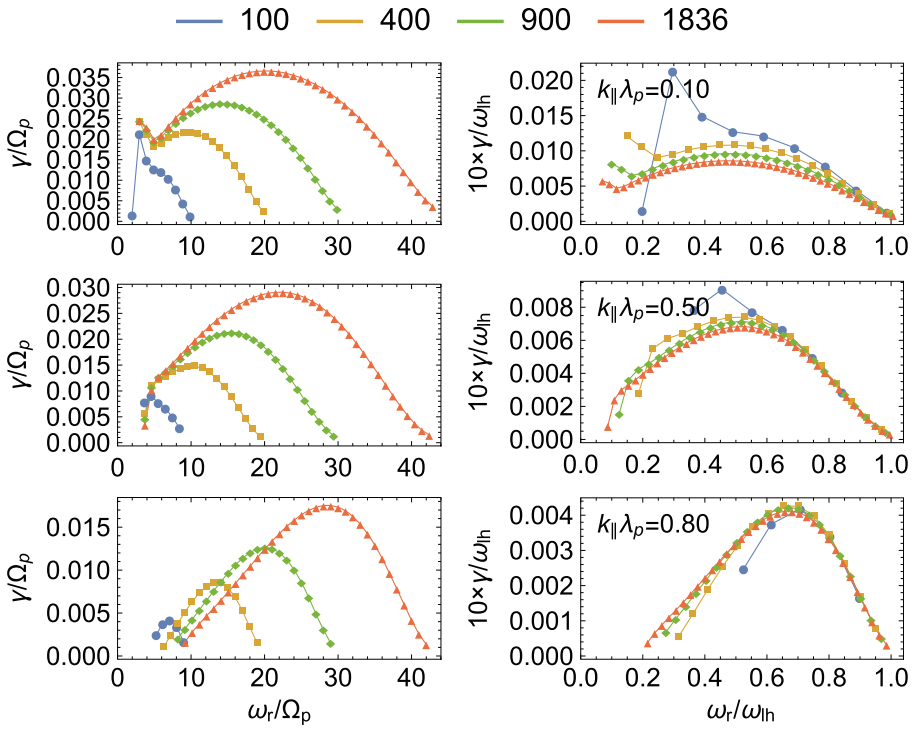

Figure 6. Comparison of the linear growth rates driven by the shell model with $v_s/v_A = 2$ (constant $k_\parallel$ slices from Figure 2). The format is the same as Figure 4 except for the different $k_\parallel$ slices as labeled.

To explain the second feature, we employ equations (A45) and (A28) which give the approximate growth rate formulae in the electron scale for $k_\parallel = 0$ and $k_\parallel \neq 0$, respectively. Although it is difficult to derive closed forms of the integrals in equations (A45) and (A28) for the ring model, assuming that $\omega_r/\Omega_p \gg 1$ and $v_r/\theta_r \gtrsim 1$, one can qualitatively explain the convergence of γ/ω_{lh} with increasing $k_\parallel$. Since $\partial f_r/\partial v_\perp \approx 0$ except in the vicinity of $v_\perp = v_r$, the Bessel function argument is large in the integral interval from which the most contribution to instability comes. Therefore, $J_j^2(x)$ may be expanded about x for a large argument and approximated by the lowest-order term [*Arfken*, 1985, pp. 573–596]:

$$J_j^2(x) \sim \frac{2}{\pi x}\cos^2\left(\frac{\pi}{4}+\frac{j\pi}{2}-x\right). \tag{3}$$

On the other hand, the terms other than the first term in F_r in equation (A8) may be neglected, assuming that the maximum growth rate occurs when the parallel resonant speed is close to zero (i.e., when $\omega_r \approx l\Omega_p$). Then by substituting equation (3) and $F_r \sim (\omega_r/k_\parallel)(\partial f_r/\partial v_\perp)$ into equations (A45) and (A28), the growth rate normalized to ω_{lh} may be determined by

$$\begin{cases} \frac{\gamma^2}{\omega_{lh}^2} \propto \int_0^\infty \frac{\omega_r^2\Omega_p}{k_\perp^3}\cos^2(\cdots)\frac{\partial H_r}{v_\perp \partial v_\perp}dv_\perp & \text{for } k_\parallel = 0 \\ \frac{\gamma}{\omega_{lh}} \propto \int_0^\infty \frac{\omega_r^3}{k_\parallel k_\perp^3}\cos^2(\cdots)\frac{\partial f_r}{v_\perp \partial v_\perp}dv_\perp & \text{for } k_\parallel \neq 0 \end{cases}, \tag{4}$$

where $(\cdots)$ denotes the cosine argument from equation (3), $l\Omega_p$ is replaced with ω_r, and only the $j = l$ term is kept in the summation of equation (A28) for the $k_\parallel \neq 0$ case. Note that the terms before the integrals in equations (A45) and (A28) (especially for the $k_\parallel \neq 0$ case) are independent of m_p/m_e (and c/v_A) for fixed ω_r/ω_{lh} and $k_\parallel\lambda_p$ and therefore are omitted for brevity. Since the cosine term is a highly oscillating function, it is clear that γ/ω_{lh} is inversely proportional to $(m_p/m_e)^{1/4}$ for $k_\parallel = 0$ but relatively constant for $k_\parallel \neq 0$ (again for fixed ω_r/ω_{lh}). Note that if normalized to Ω_p, γ from equation (4) will increase with increasing m_p/m_e which explains the overall growth rate increases shown in Figures 1 and 2 when m_p/m_e becomes large. In addition, unlike the sharp contrast between the $k_\parallel = 0$ and $k_\parallel \neq 0$ cases suggested by equation (4), the full linear theory results

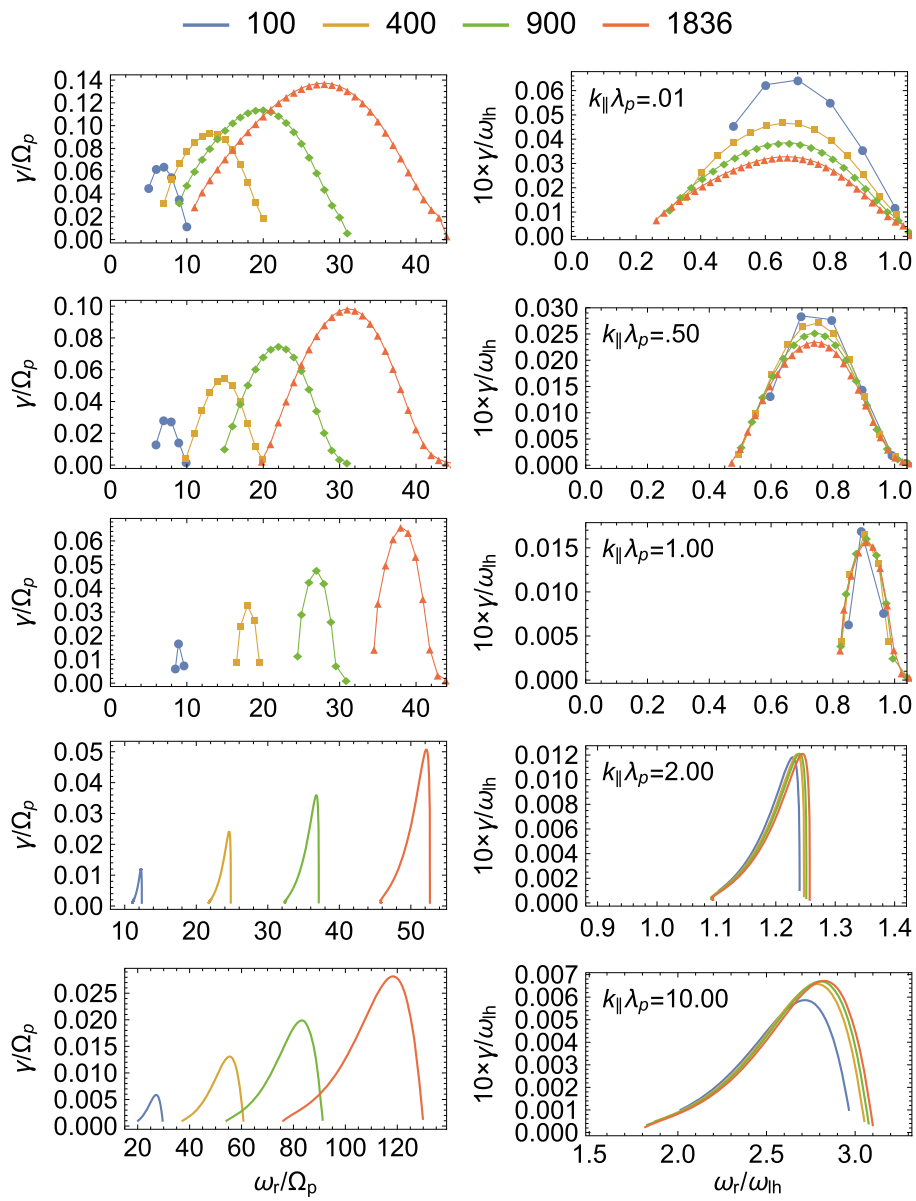

Figure 7. Comparison of the linear growth rates driven by the ring model with $v_r/v_A = 1.2$ for $c/v_A = 200$. The format is the same as Figure 5.

exhibit a smooth transition of the γ/ω_{lh} scaling property as $k_\parallel$ increases (e.g., Figure 5, right column). This transition is probably related to the change of the cyclotron resonant interaction mechanism—whether or not the Doppler effect is involved (between nonresonance for $k_\parallel = 0$ and resonance for $k_\parallel \neq 0$ according to *Chen* [2015]).

4. Conclusions and Discussions

We have investigated how the linear dispersion properties of ion Bernstein instabilities vary with the proton-to-electron mass ratio, m_p/m_e, for a sufficiently large light-to-Alfvén speed ratio, c/v_A, assuming two different types of tenuous energetic proton velocity distributions, namely, ring and shell distributions. Comparison of the real frequencies, ω_r, for different values of m_p/m_e indicates that there exist two scaling factors depending on the importance of electron kinetic effects. The dispersion relations of the unstable modes with $\omega_r \sim \Omega_p$ and $k\lambda_p \sim 1$ become independent of m_p/m_e when the real frequency and wave number are normalized to Ω_p and λ_p^{-1}, respectively, and this regime is labeled as proton kinetic scale limit where the influence of

electrons can be neglected. In contrast, the dispersion relations of the unstable modes with $\Omega_p \ll \omega_r \lesssim \omega_{lh}$ and $\lambda_p^{-1} \ll k \lesssim \lambda_e^{-1}$ become independent of m_p/m_e when the real frequency and wave number are normalized to $\omega_{\rm lh}$ and λ_e^{-1}, respectively, and this regime is labeled as electron kinetic scale limit. As for the growth rates, γ/Ω_p is roughly independent of m_p/m_e regardless of propagation direction in the proton kinetic scale limit. In the electron scale limit, however, $\gamma/\omega_{\rm lh}$ is roughly independent of m_p/m_e for sufficiently large $k_\parallel$ but inversely proportional to $(m_p/m_e)^{1/4}$ for $k_\parallel \approx 0$. This $\gamma/\omega_{\rm lh}$ scaling property transitions smoothly with $k_\parallel$ and seems to be associated with the change of the resonant interaction mechanism.

The present study is limited to sufficiently large c/v_A such that $\omega_{pe}^2/\Omega_e^2 = (m_e/m_p)(c/v_A)^2 \gg 1$. *Boardsen et al.* [2016] recently reported a thorough study of frequency-dependent fast magnetosonic wave modes based on satellite data worth of 2 years. From Figure 14 therein and assuming a dipole geomagnetic field, it appears that $c/v_A = 400$ assumed here is close to the upper limit of the c/v_A values associated with fast magnetosonic waves observed. On the other hand, the lower limit of c/v_A is near 200. To explore how the change of c/v_A may affect the results, we carried out one set of calculation using the ring model with $c/v_A = 200$ and $v_r = 1.2v_A$ which will lead to wave growth only at the electron scale limit. The result is shown in Figure 7 and is very consistent with Figure 5, i.e., with the $c/v_A = 400$ case. Combined with the approximate growth rate formula derivation described in Appendix A, the agreement between Figures 5 and 7 suggests that the instability is insensitive to the change of c/v_A, as long as $(m_e/m_p)(c/v_A)^2 \gg 1$ is satisfied.

Boardsen et al. [2016] also showed that the observed ratios of the electric field wave amplitude to the magnetic field wave amplitude are consistent with those of the cold plasma extraordinary mode, indicating that the cold plasma assumption made to explain the aforementioned results was appropriate. A noteworthy result in their study is that the equatorial wave normal angle distribution has a frequency dependence; the median approaches 90°as ω_r increases. *Min and Liu* [2016a], using reduced m_p/m_e, showed that when the proton velocity distribution approaches a shell, the fast magnetosonic wave growth becomes more limited to the quasi-perpendicular propagation direction. Furthermore, the growth rate pattern is better organized in $k_\parallel$-$k_\perp$ space, so the higher the real frequency, the closer the wave normal angle is to 90°. The present results show that as m_p/m_e increases, the unstable $k_\perp$ range increases, while the unstable $k_\parallel$ range remains relatively unchanged. Therefore, the wave growth is further confined to quasi-perpendicular direction with increasing real frequency for realistic m_p/m_e. As suggested by *Min et al.* [2016] and consistent with the statistical result by *Boardsen et al.* [2016], the proton velocity distribution associated with the observed waves may be close to a shell distribution.

Appendix A: Approximate Growth Rate Formulae

Derived in this section is a series of approximate linear growth rate formulae considering two limiting cases: (1) $\Omega_p \ll \omega_r < \omega_{\rm lh}$ (electron kinetic scale) and (2) $\Omega_p \lesssim \omega_r \ll \omega_{\rm lh}$ (proton kinetic scale). The derivation assumes that the dispersion relation is determined by the dominant cold plasma components, while the growth rate is treated as a minor perturbation from the tenuous energetic plasma components [*Kennel*, 1966; *Chen et al.*, 2010b, 2010a]. That is, we start from the full kinetic dispersion relation and drop terms that become small in the small temperature and small growth rate limits. The approximate linear theory is justified for $|\gamma| \ll \omega_r$ and, for our model distributions, for $n_{r,s} \ll n_c \approx n_e$, and $\tilde{\beta}_{c,e} \ll 1$.

A1. For $k_\parallel \neq 0$ Case

In this subsection, we derive the approximate linear growth rate formulae for quasi-perpendicular propagating modes. We begin with a general form of kinetic linear dispersion theory for electromagnetic fluctuations in a homogeneous, magnetized, collisionless plasma [e.g., *Umeda et al.*, 2012]

$$0 = D(\omega, \mathbf{k}) \equiv \begin{vmatrix} \epsilon_{xx} - \frac{k_\parallel^2 c^2}{\omega^2} & \epsilon_{xy} & \epsilon_{xz} + \frac{k_\parallel k_\perp c^2}{\omega^2} \\ -\epsilon_{xy} & \epsilon_{yy} - \frac{k^2 c^2}{\omega^2} & \epsilon_{yz} \\ \epsilon_{xz} + \frac{k_\parallel k_\perp c^2}{\omega^2} & -\epsilon_{yz} & \epsilon_{zz} - \frac{k_\perp^2 c^2}{\omega^2} \end{vmatrix}, \tag{A1}$$

where the dielectric components are

$$\epsilon_{xx} = 1 + 2\pi \sum_\sigma \frac{\omega_{p\sigma}^2}{\omega^2} \sum_{j=-\infty}^{\infty} \frac{j^2 \Omega_\sigma^2}{k_\perp^2} \int_0^\infty dv_\perp J_j^2 \int_{-\infty}^\infty \frac{k_\parallel dv_\parallel}{\omega - k_\parallel v_\parallel - j\Omega_\sigma} F_\sigma, \tag{A2}$$

$$\epsilon_{yy} = 1 + 2\pi \sum_{\sigma} \frac{\omega_{p\sigma}^2}{\omega^2} \sum_{j=-\infty}^{\infty} \int_0^{\infty} \mathrm{d}v_{\perp} v_{\perp}^2 (J_j')^2 \int_{-\infty}^{\infty} \frac{k_{\parallel} \mathrm{d}v_{\parallel}}{\omega - k_{\parallel} v_{\parallel} - j\Omega_{\sigma}} F_{\sigma}, \tag{A3}$$

$$\epsilon_{xy} = 2\pi i \sum_{\sigma} \frac{\omega_{p\sigma}^2}{\omega^2} \sum_{j=-\infty}^{\infty} \frac{j\Omega_{\sigma}}{k_{\perp}} \int_0^{\infty} \mathrm{d}v_{\perp} v_{\perp} J_j J_j' \int_{-\infty}^{\infty} \frac{k_{\parallel} \mathrm{d}v_{\parallel}}{\omega - k_{\parallel} v_{\parallel} - j\Omega_{\sigma}} F_{\sigma}, \tag{A4}$$

$$\epsilon_{xz} = 2\pi \sum_{\sigma} \frac{\omega_{p\sigma}^2}{\omega^2} \sum_{j=-\infty}^{\infty} \frac{j\Omega_{\sigma}}{k_{\perp}} \int_0^{\infty} \mathrm{d}v_{\perp} J_j^2 \int_{-\infty}^{\infty} \frac{k_{\parallel} v_{\parallel} \mathrm{d}v_{\parallel}}{\omega - k_{\parallel} v_{\parallel} - j\Omega_{\sigma}} G_{\sigma}, \tag{A5}$$

$$\epsilon_{yz} = -2\pi i \sum_{\sigma} \frac{\omega_{p\sigma}^2}{\omega^2} \sum_{j=-\infty}^{\infty} \int_0^{\infty} \mathrm{d}v_{\perp} v_{\perp} J_j J_j' \int_{-\infty}^{\infty} \frac{k_{\parallel} v_{\parallel} \mathrm{d}v_{\parallel}}{\omega - k_{\parallel} v_{\parallel} - j\Omega_{\sigma}} G_{\sigma}, \text{ and} \tag{A6}$$

$$\epsilon_{zz} = 1 + 2\pi \sum_{\sigma} \frac{\omega_{p\sigma}^2}{\omega^2} \sum_{j=-\infty}^{\infty} \int_0^{\infty} \mathrm{d}v_{\perp} J_j^2 \int_{-\infty}^{\infty} \frac{k_{\parallel} v_{\parallel}^2 \mathrm{d}v_{\parallel}}{\omega - k_{\parallel} v_{\parallel} - j\Omega_{\sigma}} G_{\sigma}. \tag{A7}$$

Here σ denotes the plasma component, $J_j(k_{\perp} v_{\perp}/\Omega_{\sigma})$ is the Bessel function of the first kind with an integer j, $J_j'(x) = \mathrm{d}J_j(x)/\mathrm{d}x$ and

$$F_{\sigma} \equiv \frac{\omega}{k_{\parallel}} \frac{\partial f_{\sigma}}{\partial v_{\perp}} - v_{\parallel} \frac{\partial f_{\sigma}}{\partial v_{\perp}} + v_{\perp} \frac{\partial f_{\sigma}}{\partial v_{\parallel}} \text{ and } G_{\sigma} \equiv \frac{j\Omega_{\sigma}}{k_{\parallel}} \frac{\partial f_{\sigma}}{\partial v_{\perp}} + \frac{\omega - j\Omega_{\sigma}}{k_{\parallel}} \frac{v_{\perp}}{v_{\parallel}} \frac{\partial f_{\sigma}}{\partial v_{\parallel}}. \tag{A8}$$

Paper 1 neglected ϵ_{xz} and ϵ_{yz} in equation (A1), which may be sufficient for small $k_{\parallel}$. Here they will be kept because the range of $k_{\parallel}$ under consideration can be sufficiently large.

Following the same step as in paper 1, we separate D into the two lowest order contributions:

$$\begin{aligned} D^{(0)} &= \left((\epsilon_{xy}^{(0)})^2 + \epsilon_{xx}^{(0)} \epsilon_{yy}^{(0)} - \epsilon_{xx}^{(0)} \frac{k_{\perp}^2 c^2}{\omega^2} \right) \left(\epsilon_{zz}^{(0)} - \frac{k_{\perp}^2 c^2}{\omega^2} \right) + \epsilon_{zz}^{(0)} \frac{k_{\parallel}^4 c^4}{\omega^4} \\ &\quad - \frac{k_{\parallel}^2 c^2}{\omega^2} \left(\left(\epsilon_{xx}^{(0)} + \epsilon_{yy}^{(0)} \right) \epsilon_{zz}^{(0)} - \left(\epsilon_{xx}^{(0)} + \epsilon_{zz}^{(0)} \right) \frac{k_{\perp}^2 c^2}{\omega^2} \right) \\ &= \left[(\epsilon_{xy}^{(0)})^2 + \left(\epsilon_{xx}^{(0)} - \frac{k_{\parallel}^2 c^2}{\omega^2} \right) \left(\epsilon_{yy}^{(0)} - \frac{k^2 c^2}{\omega^2} \right) \right] \left(\epsilon_{zz}^{(0)} - \frac{k_{\perp}^2 c^2}{\omega^2} \right) - \frac{k_{\parallel}^2 k_{\perp}^2 c^4}{\omega^4} \left(\epsilon_{yy}^{(0)} - \frac{k^2 c^2}{\omega^2} \right), \end{aligned} \tag{A9}$$

and

$$\begin{aligned} D^{(1)} &= \left(\epsilon_{yy}^{(0)} - \frac{k^2 c^2}{\omega^2} \right) \left(\epsilon_{zz}^{(0)} - \frac{k_{\perp}^2 c^2}{\omega^2} \right) \epsilon_{xx}^{(1)} + \left[\left(\epsilon_{xx}^{(0)} - \frac{k_{\parallel}^2 c^2}{\omega^2} \right) \epsilon_{zz}^{(0)} - \epsilon_{xx}^{(0)} \frac{k_{\perp}^2 c^2}{\omega^2} \right] \epsilon_{yy}^{(1)} \\ &\quad + \left[(\epsilon_{xy}^{(0)})^2 + \left(\epsilon_{xx}^{(0)} - \frac{k_{\parallel}^2 c^2}{\omega^2} \right) \left(\epsilon_{yy}^{(0)} - \frac{k^2 c^2}{\omega^2} \right) \right] \epsilon_{zz}^{(1)} \\ &\quad + 2\epsilon_{xy}^{(0)} \left(\epsilon_{zz}^{(0)} - \frac{k_{\perp}^2 c^2}{\omega^2} \right) \epsilon_{xy}^{(1)} - 2 \frac{k_{\parallel} k_{\perp} c^2}{\omega^2} \left(\epsilon_{yy}^{(0)} - \frac{k^2 c^2}{\omega^2} \right) \epsilon_{xz}^{(1)} + 2 \frac{k_{\parallel} k_{\perp} c^2}{\omega^2} \epsilon_{xy}^{(0)} \epsilon_{yz}^{(1)}, \end{aligned} \tag{A10}$$

where $D^{(0)}$ is real and denotes the zero-temperature core plasma components' contribution to D, and $D^{(1)}$ is complex and denotes the energetic proton component's contribution. Then the real frequency (ω_r) and the growth rate (γ) can be obtained respectively from [*Kennel*, 1966]

$$D^{(0)}(\omega_r, \mathbf{k}) = 0 \text{ and } \gamma = - \left. \frac{\Im D^{(1)}(\omega, \mathbf{k})}{\partial D^{(0)}/\partial \omega} \right|_{\omega = \omega_r}. \tag{A11}$$

For our assumed model distributions, the lowest-order zero-temperature dielectric components can be obtained by following the derivation of the cold plasma dispersion relation [e.g., *Stix*, 1992; *Min and Liu*, 2016a]:

$$\epsilon_{xx}^{(0)} = \epsilon_{yy}^{(0)} = 1 - \frac{1}{2} \sum_{\sigma = e,c} \frac{\omega_{p\sigma}^2}{\omega^2} \sum_{\pm} \frac{\omega}{\omega \mp \Omega_{\sigma}}, \tag{A12}$$

$$\epsilon_{xy}^{(0)} = \frac{i}{2}\sum_{\sigma=e,c}\frac{\omega_{p\sigma}^2}{\omega^2}\sum_{\pm}\mp\frac{\omega}{\omega\mp\Omega_\sigma}, \tag{A13}$$

$$\epsilon_{zz}^{(0)} = 1-\sum_{\sigma=e,c}\frac{\omega_{p\sigma}^2}{\omega^2}, \tag{A14}$$

and, for nondrifting plasma components assumed, $\epsilon_{xz}^{(0)} = \epsilon_{yz}^{(0)} = 0$. Note that in equation (A9), terms with the latter two components have already been neglected. From equations (A2)–(A7) and noting that the imaginary part of equation (A10) contributes to γ, the first-order dielectric components which contribute to γ read

$$\mathfrak{F}\epsilon_{xx}^{(1)} \approx -2\pi^2\frac{\omega_{p\sigma}^2}{\omega^2}\sum_{j=-\infty}^{\infty}\int_0^\infty \mathrm{d}v_\perp \frac{j^2\Omega_\sigma^2}{k_\perp^2}J_j^2F_\sigma\Big|_{v_\parallel=v_{j,\mathrm{res}}}, \tag{A15}$$

$$\mathfrak{F}\epsilon_{yy}^{(1)} \approx -2\pi^2\frac{\omega_{p\sigma}^2}{\omega^2}\sum_{j=-\infty}^{\infty}\int_0^\infty \mathrm{d}v_\perp v_\perp^2(J_j')^2F_\sigma\Big|_{v_\parallel=v_{j,\mathrm{res}}}, \tag{A16}$$

$$\mathfrak{R}\epsilon_{xy}^{(1)} \approx 2\pi^2\frac{\omega_{p\sigma}^2}{\omega^2}\sum_{j=-\infty}^{\infty}\int_0^\infty \mathrm{d}v_\perp \frac{j\Omega_\sigma}{k_\perp}v_\perp J_jJ_j'F_\sigma\Big|_{v_\parallel=v_{j,\mathrm{res}}}, \tag{A17}$$

$$\mathfrak{F}\epsilon_{xz}^{(1)} \approx -2\pi^2\frac{\omega_{p\sigma}^2}{\omega^2}\sum_{j=-\infty}^{\infty}\int_0^\infty \mathrm{d}v_\perp v_\parallel \frac{j\Omega_\sigma}{k_\perp}J_j^2G_\sigma\Big|_{v_\parallel=v_{j,\mathrm{res}}}, \tag{A18}$$

$$\mathfrak{R}\epsilon_{yz}^{(1)} \approx -2\pi^2\frac{\omega_{p\sigma}^2}{\omega^2}\sum_{j=-\infty}^{\infty}\int_0^\infty \mathrm{d}v_\perp v_\parallel v_\perp J_jJ_j'G_\sigma\Big|_{v_\parallel=v_{j,\mathrm{res}}}, \tag{A19}$$

$$\mathfrak{F}\epsilon_{zz}^{(1)} \approx -2\pi^2\frac{\omega_{p\sigma}^2}{\omega^2}\sum_{j=-\infty}^{\infty}\int_0^\infty \mathrm{d}v_\perp v_\parallel^2J_j^2G_\sigma\Big|_{v_\parallel=v_{j,\mathrm{res}}}, \tag{A20}$$

where $v_{j,\mathrm{res}} \equiv (\omega - j\Omega_\sigma)/k_\parallel$ is the parallel resonant speed and σ in this case denotes the energetic proton component (either ring or shell). In deriving these dielectric components, the integrations in the parallel velocity component are carried out on the real axis for the principal values of the integrals [e.g., *Chen et al.*, 2013, equation (4)].

By substituting the relevant terms into equation (A11) and noting that $G_\sigma = F_\sigma$ when $v_\parallel = v_{j,\mathrm{res}}$, the growth rate can read

$$\gamma = \frac{2\pi^2}{\partial D^{(0)}/\partial\omega_r}\frac{\omega_{p\sigma}^2}{\omega_r^2}\sum_{j=-\infty}^{\infty}\int_0^\infty \mathrm{d}v_\perp WF_\sigma\Big|_{v_\parallel=v_{j,\mathrm{res}}}, \tag{A21}$$

where W is defined as

$$\begin{aligned} W \equiv{}& \left(\epsilon_{yy}^{(0)}-\frac{k^2c^2}{\omega_r^2}\right)\left(\epsilon_{zz}^{(0)}-\frac{k_\perp^2c^2}{\omega_r^2}\right)\frac{j^2\Omega_\sigma^2}{k_\perp^2}J_j^2 + \left[\left(\epsilon_{xx}^{(0)}-\frac{k_\parallel^2c^2}{\omega_r^2}\right)\epsilon_{zz}^{(0)}-\epsilon_{xx}^{(0)}\frac{k_\perp^2c^2}{\omega_r^2}\right]v_\perp^2(J_j')^2 \\ &-2(\epsilon_{xy}^{(0)}/i)\left(\epsilon_{zz}^{(0)}-\frac{k_\perp^2c^2}{\omega_r^2}\right)\frac{j\Omega_\sigma}{k_\perp}v_\perp J_jJ_j' - 2\frac{k_\parallel k_\perp c^2}{\omega_r^2}\left(\epsilon_{yy}^{(0)}-\frac{k^2c^2}{\omega_r^2}\right)v_\parallel\frac{j\Omega_\sigma}{k_\perp}J_j^2 \\ &+\left[(\epsilon_{xy}^{(0)})^2+\left(\epsilon_{xx}^{(0)}-\frac{k_\parallel^2c^2}{\omega_r^2}\right)\left(\epsilon_{yy}^{(0)}-\frac{k^2c^2}{\omega_r^2}\right)\right]v_\parallel^2J_j^2 + 2\frac{k_\parallel k_\perp c^2}{\omega_r^2}(\epsilon_{xy}^{(0)}/i)v_\parallel v_\perp J_jJ_j'. \end{aligned} \tag{A22}$$

Now we further simplify γ assuming the two limiting cases corresponding to the electron and proton kinetic scales, respectively. Let us first consider the first case. With a further assumption that $\omega_{pe}^2/\Omega_e^2 \equiv$

$(m_e/m_p)(c/v_A)^2 \gg 1$, the lower hybrid frequency can be expressed as $\omega_{lh} \approx \Omega_p\sqrt{m_p/m_e}$, and the dielectric components (A12–A14) may be approximated to the lowest order of m_e/m_p with

$$\epsilon_{xx}^{(0)} \approx 1 - \frac{m_e}{m_p}\frac{c^2}{v_A^2}\left(\frac{\omega_{lh}^2}{\omega_r^2} - 1\right),\ \epsilon_{xy}^{(0)} \approx -i\sqrt{\frac{m_e}{m_p}}\frac{c^2}{v_A^2}\frac{\omega_{lh}}{\omega_r} \text{ and } \epsilon_{zz}^{(0)} \approx 1 - \frac{c^2}{v_A^2}\frac{\omega_{lh}^2}{\omega_r^2} \approx -\frac{c^2}{v_A^2}\frac{\omega_{lh}^2}{\omega_r^2}. \tag{A23}$$

Based on the relative order $\epsilon_{zz}^{(0)} \sim k_\perp^2c^2/\omega^2 \gg \epsilon_{xx}^{(0)}$ and $k_\perp \gg k_\parallel$, the first form of $D^{(0)}$ in equation (A9) may be simplified to

$$\begin{aligned} D^{(0)} &\approx \left((\epsilon_{xy}^{(0)})^2 - \epsilon_{xx}^{(0)}\frac{k_\perp^2c^2}{\omega_r^2}\right)\left(\epsilon_{zz}^{(0)} - \frac{k_\perp^2c^2}{\omega_r^2}\right) + \frac{k_\parallel^2k_\perp^2c^4}{\omega_r^4}\epsilon_{zz}^{(0)} \\ &= \frac{m_e}{m_p}\frac{c^2}{v_A^2}\left(\frac{c^2}{v_A^2}\frac{\omega_{lh}^2}{\omega_r^2} + \frac{k_\perp^2c^2}{\omega_r^2}\right)\left[\frac{c^2}{v_A^2}\frac{\omega_{lh}^2}{\omega_r^2} + \frac{k_\perp^2c^2}{\omega_r^2}\left(1 + \frac{m_p}{m_e}\frac{v_A^2}{c^2} - \frac{\omega_{lh}^2}{\omega_r^2}\right)\right] - \frac{c^2}{v_A^2}\frac{\omega_{lh}^2}{\omega_r^2}\frac{k_\parallel^2k_\perp^2c^4}{\omega_r^4} \\ &\approx \frac{m_e}{m_p}\frac{c^2}{v_A^2}\left(\frac{c^2}{v_A^2}\frac{\omega_{lh}^2}{\omega_r^2} + \frac{k_\perp^2c^2}{\omega_r^2}\right)\left[\frac{c^2}{v_A^2}\frac{\omega_{lh}^2}{\omega_r^2} + \frac{k_\perp^2c^2}{\omega_r^2}\left(1 - \frac{\omega_{lh}^2}{\omega_r^2}\right)\right] - \frac{c^2}{v_A^2}\frac{\omega_{lh}^2}{\omega_r^2}\frac{k_\parallel^2k_\perp^2c^4}{\omega_r^4}. \end{aligned} \tag{A24}$$

Note that $(m_e/m_p)(c/v_A)^2 \gg 1$ has been used to derive the final form. By solving $D^{(0)} = 0$ for $k_\perp^2c^2/\omega_r^2$, the approximate cold plasma dispersion relation is given by

$$\frac{k_\perp^2c^2}{\omega_r^2} \approx \frac{c^2/v_A^2}{2(\omega_r^2/\omega_{lh}^2 - 1)}\left[-2 + (1 + k_\parallel^2\lambda_p^2)\frac{\omega_{lh}^2}{\omega_r^2} - \frac{\omega_{lh}}{\omega_r}\sqrt{(1 + k_\parallel^2\lambda_p^2)^2\frac{\omega_{lh}^2}{\omega_r^2} - 4k_\parallel^2\lambda_p^2}\right], \tag{A25}$$

and the approximate derivative $\partial D^{(0)}/\partial\omega_r$ needed for the growth rate is given by

$$\frac{\partial D^{(0)}}{\partial\omega_r} \approx -\frac{4}{\omega_r}\frac{m_e}{m_p}\frac{c^2}{v_A^2}\left[\frac{c^4}{v_A^4}\frac{\omega_{lh}^4}{\omega_r^4} + \left(1 - \frac{3}{2}\frac{\omega_{lh}^2}{\omega_r^2}\right)\frac{k_\perp^4c^4}{\omega_r^4} + \left(2 - \frac{3(1 + k_\parallel^2\lambda_p^2)}{2}\frac{\omega_{lh}^2}{\omega_r^2}\right)\frac{c^2}{v_A^2}\frac{\omega_{lh}^2}{\omega_r^2}\frac{k_\perp^2c^2}{\omega_r^2}\right]. \tag{A26}$$

Similarly based on the relative order, the weighting function is mainly determined by the first term in equation (A22):

$$W \approx \frac{k^2c^2}{\omega_r^2}\left(\frac{k_\perp^2c^2}{\omega_r^2} - \epsilon_{zz}^{(0)}\right)\frac{j^2\Omega_\sigma^2}{k_\perp^2}J_j^2, \tag{A27}$$

where $\epsilon_{yy}^{(0)}$ has been neglected compared to k^2c^2/ω_r^2. Finally, putting all relevant terms together, the approximate growth rate formula corresponding to the electron kinetic scale regime may read

$$\begin{aligned} \frac{\gamma}{\omega_{lh}} &\approx -\frac{\pi^2\frac{n_\sigma}{n_0}\frac{\omega_{lh}}{\omega_r}}{2[\cdots]}\frac{k^2c^2}{\omega_r^2}\left(\frac{k_\perp^2c^2}{\omega_r^2} - \epsilon_{zz}^{(0)}\right)\sum_{j=-\infty}^{\infty}\int_0^\infty \mathrm{d}v_\perp\frac{j^2\Omega_\sigma^2}{k_\perp^2}J_j^2F_\sigma\Big|_{v_\parallel = v_{j,\mathrm{res}}} \\ &= -\frac{\frac{\pi^2}{2}\frac{n_\sigma}{n_0}\frac{\omega_{lh}}{\omega_r}\frac{k^2v_A^2}{\omega_r^2}\left(\frac{k_\perp^2v_A^2}{\omega_r^2} + \frac{\omega_{lh}^2}{\omega_r^2}\right)}{\frac{\omega_{lh}^4}{\omega_r^4} + \left(1 - \frac{3}{2}\frac{\omega_{lh}^2}{\omega_r^2}\right)\frac{k_\perp^4v_A^4}{\omega_r^4} + \left(2 - \frac{3(1+k_\parallel^2\lambda_p^2)}{2}\frac{\omega_{lh}^2}{\omega_r^2}\right)\frac{\omega_{lh}^2}{\omega_r^2}\frac{k_\perp^2v_A^2}{\omega_r^2}}\sum_{j=-\infty}^{\infty}\int_0^\infty \mathrm{d}v_\perp\frac{j^2\Omega_\sigma^2}{k_\perp^2}J_j^2F_\sigma\Big|_{v_\parallel = v_{j,\mathrm{res}}}, \end{aligned} \tag{A28}$$

where $[\cdots]$ denotes the term within the square bracket in equation (A26). Although we could not further simplify the term in front of the summation, it is independent of m_p/m_e and c/v_A for fixed ω_r/ω_{lh} and $k_\parallel\lambda_p$.

The growth rate formula corresponding to the proton scale regime is simpler. By following similar steps, the dielectric components (A12–A14) can be expressed to the lowest order of m_e/m_p as

$$\epsilon_{xx}^{(0)} \approx -\frac{c^2}{v_A^2}\frac{\Omega_p^2}{\omega_r^2 - \Omega_p^2},\ \epsilon_{xy}^{(0)} \approx -i\frac{c^2}{v_A^2}\frac{\omega_r\Omega_p}{\omega_r^2 - \Omega_p^2} \text{ and } \epsilon_{zz}^{(0)} \approx -\frac{m_p}{m_e}\frac{c^2}{v_A^2}\frac{\Omega_p^2}{\omega_r^2}. \tag{A29}$$

Considering the relative order $\epsilon_{zz}^{(0)} \gg \epsilon_{xx}^{(0)} \sim k_\perp^2c^2/\omega^2 \gtrsim k_\parallel^2c^2/\omega^2$, the second form of $D^{(0)}$ in equation (A9) may be simplified to

$$D^{(0)} \approx \left[(\epsilon_{xy}^{(0)})^2 + \left(\epsilon_{xx}^{(0)} - \frac{k_\parallel^2c^2}{\omega^2}\right)\left(\epsilon_{yy}^{(0)} - \frac{k^2c^2}{\omega^2}\right)\right]\epsilon_{zz}^{(0)}. \tag{A30}$$

By solving $D^{(0)} = 0$ for k^2c^2/ω_r^2, the approximate cold plasma dispersion relation is given by

$$\frac{k^2c^2}{\omega_r^2} \approx \frac{c^2}{v_A^2}\frac{\omega_r^2 - k_\parallel^2 v_A^2}{(1+k_\parallel^2\lambda_p^2)\omega_r^2 - k_\parallel^2 v_A^2}, \tag{A31}$$

and the approximate derivative $\partial D^{(0)}/\partial\omega_r$ is given by

$$\begin{aligned}\frac{\partial D^{(0)}}{\partial\omega_r} &\approx -2\frac{\epsilon_{zz}^{(0)}}{\omega_r}\frac{c^4}{v_A^4}\frac{\Omega_p^2}{\omega_r^2(\omega_r^2-\Omega_p^2)}\frac{(1+k_\parallel^2\lambda_p^2)\omega_r^4 - (2\omega_r^2 - k_\parallel^2 v_A^2)k_\parallel^2 v_A^2}{(1+k_\parallel^2\lambda_p^2)\omega_r^2 - k_\parallel^2 v_A^2} \\ &\approx -2\frac{\epsilon_{zz}^{(0)}}{\omega_r}\frac{c^4}{v_A^4}\frac{\Omega_p^2}{\omega_r^2-\Omega_p^2}\frac{(1+k_\parallel^2\lambda_p^2)\omega_r^2 - 2k_\parallel^2 v_A^2}{(1+k_\parallel^2\lambda_p^2)\omega_r^2 - k_\parallel^2 v_A^2}.\end{aligned} \tag{A32}$$

Similarly, the weighting function is determined by the terms involving $\epsilon_{zz}^{(0)}$ in equation (A22):

$$\begin{aligned}W &\approx -\epsilon_{zz}^{(0)}\left(\frac{k^2c^2}{\omega_r^2} - \epsilon_{yy}^{(0)}\right)\frac{j^2\Omega_\sigma^2}{k_\perp^2}J_j^2 - \epsilon_{zz}^{(0)}\left(\frac{k_\parallel^2c^2}{\omega_r^2} - \epsilon_{xx}^{(0)}\right)v_\perp^2(J_j')^2 - 2(\epsilon_{xy}^{(0)}/i)\epsilon_{zz}^{(0)}\frac{j\Omega_\sigma}{k_\perp}v_\perp J_j J_j' \\ &= -\epsilon_{zz}^{(0)}\left[\sqrt{\frac{k^2c^2}{\omega_r^2} - \epsilon_{yy}^{(0)}}\frac{j\Omega_\sigma}{k_\perp}J_j - \sqrt{\frac{k_\parallel^2c^2}{\omega_r^2} - \epsilon_{xx}^{(0)}}v_\perp J_j'\right]^2.\end{aligned} \tag{A33}$$

The second form has been derived using $D^{(0)} = 0$ with equation (A30) and by taking into account the fact that $\Re\epsilon_{xx}^{(0)}$ and $\Im\epsilon_{xy}^{(0)}$ are negative for $\omega_r > \Omega_p$ as suggested by equation (A29). After substituting the relevant terms, the approximate growth rate formula reads

$$\begin{aligned}\frac{\gamma}{\Omega_p} \approx{}& \pi^2\frac{n_\sigma}{n_0}\frac{\Omega_p}{\omega_r}\frac{(1+k_\parallel^2\lambda_p^2)\omega_r^2 - k_\parallel^2 v_A^2}{(1+k_\parallel^2\lambda_p^2)\omega_r^2 - 2k_\parallel^2 v_A^2} \\ &\sum_{j=-\infty}^{\infty}\int_0^\infty dv_\perp\left[\sqrt{\frac{k^2v_A^2}{\omega_r^2}\frac{\omega_r^2-\Omega_p^2}{\Omega_p^2}+1}\frac{j\Omega_\sigma}{k_\perp}J_j - \sqrt{\frac{k_\parallel^2v_A^2}{\omega_r^2}\frac{\omega_r^2-\Omega_p^2}{\Omega_p^2}+1}v_\perp J_j'\right]^2 F_\sigma\Big|_{v_\parallel = v_{j,res}}.\end{aligned} \tag{A34}$$

A2. For $k_\parallel = 0$ Case

In this subsection, we derive the approximate linear growth rate formulae valid for $k_\parallel = 0$. It should be noted that *Gul'elmi et al.* [1975] derived an approximate growth rate formula for $k_\parallel = 0$ in the limit $\Omega_p \ll \omega_r \le \omega_{lh}$ (i.e., electron kinetic scale) to investigate the generation mechanism of the magnetospheric ion Bernstein instability, and *Chen* [2015] recently put forth an effort to provide a more general formula encompassing the proton scale regime as well. Following *Gul'elmi et al.* [1975] and *Chen* [2015], we consider the extraordinary mode dispersion relation

$$D_\perp(\omega, k = k_\perp) = \epsilon_{xy}^2 + \epsilon_{xx}\left(\epsilon_{yy} - \frac{k^2c^2}{\omega^2}\right). \tag{A35}$$

Similar to equations (A9) and (A10), $D_\perp^{(0)}$ and $D_\perp^{(1)}$ can respectively read

$$D_\perp^{(0)} \equiv \epsilon_{xx}^{(0)}\left(\epsilon_{xx}^{(0)} - \frac{k^2c^2}{\omega^2}\right) + (\epsilon_{xy}^{(0)})^2 \text{ and} \tag{A36}$$

$$D_\perp^{(1)} \equiv \left(\epsilon_{xx}^{(0)} - \frac{k^2c^2}{\omega^2}\right)\epsilon_{xx}^{(1)} + \epsilon_{xx}^{(0)}\epsilon_{yy}^{(1)} + 2\epsilon_{xy}^{(0)}\epsilon_{xy}^{(1)}, \tag{A37}$$

where $\epsilon_{xx}^{(0)}$ and $\epsilon_{xy}^{(0)}$ are given in equations (A12) and (A13), respectively, and $\epsilon_{yy}^{(0)}$ has been replaced with $\epsilon_{xx}^{(0)}$.

The next step is to evaluate the dielectric components contributed by the energetic proton component. For $k_\parallel = 0$ the growth rates maximize at exact harmonics of Ω_p [*Gul'elmi et al.*, 1975; *Chen*, 2015] so we further assume $\omega_{r,l} \equiv l\Omega_p$, where l is a positive integer. Since the imaginary part of $\omega/(\omega - j\Omega_p)$ is the source of wave growth [*McClements and Dendy*, 1993; *Chen*, 2015], by substituting $\omega = \omega_{r,l} + i\gamma_l$ and $k_\parallel = 0$ into

equations (A2) – (A4), the lowest-order dielectric components contributing to γ_l (that is, the growth rate of the lth proton cyclotron harmonic mode) can be written as

$$\mathfrak{T}\epsilon_{xx}^{(1)} \approx -2\pi \frac{\omega_{r,l}}{\gamma_l} \frac{\omega_{p\sigma}^2}{\omega_{r,l}^2} \int_0^\infty J_l^2 \frac{l^2\Omega_p^2}{k^2} \frac{\partial H_\sigma}{\partial v_\perp} \mathrm{d}v_\perp, \tag{A38}$$

$$\mathfrak{R}\epsilon_{xy}^{(1)} \approx 2\pi \frac{\omega_{r,l}}{\gamma_l} \frac{\omega_{p\sigma}^2}{\omega_{r,l}^2} \int_0^\infty J_l J_l' \frac{l\Omega_p}{k} v_\perp \frac{\partial H_\sigma}{\partial v_\perp} \mathrm{d}v_\perp, \text{ and} \tag{A39}$$

$$\mathfrak{T}\epsilon_{yy}^{(1)} \approx -2\pi \frac{\omega_{r,l}}{\gamma_l} \frac{\omega_{p\sigma}^2}{\omega_{r,l}^2} \int_0^\infty (J_l')^2 v_\perp^2 \frac{\partial H_\sigma}{\partial v_\perp} \mathrm{d}v_\perp, \tag{A40}$$

where σ again denotes the energetic proton component and $H_\sigma \equiv \int_{-\infty}^{\infty} f_\sigma \mathrm{d}v_\parallel$ is the reduced $v_\perp$ distribution function. By substituting the relevant terms into equation (A11) and following similar steps as in the previous subsection, it is straightforward to obtain the growth rate:

$$\gamma^2 = -2\pi \frac{\omega_{r,l}}{\partial D_\perp^{(0)}/\partial \omega_r} \frac{\omega_{p\sigma}^2}{\omega_{r,l}^2} \int_0^\infty W_\perp \frac{\partial H_\sigma}{\partial v_\perp} \mathrm{d}v_\perp, \tag{A41}$$

where the weighting function $W_\perp$ is defined as

$$\begin{aligned} W_\perp &\equiv \left(\frac{k^2c^2}{\omega_{r,l}^2} - \epsilon_{xx}^{(0)} \right) \frac{l^2\Omega_p^2}{k^2} J_l^2 - \epsilon_{xx}^{(0)} v_\perp^2 (J_l')^2 + 2(\epsilon_{xy}^{(0)}/i) \frac{l\Omega_p}{k} v_\perp J_l J_l' \\ &= \left[\sqrt{\frac{k^2c^2}{\omega_{r,l}^2} - \epsilon_{xx}^{(0)}} \frac{\omega_{r,l}}{k} J_l + \mathrm{sign}(\epsilon_{xy}^{(0)}/i) \sqrt{-\epsilon_{xx}^{(0)}} v_\perp J_l' \right]^2. \end{aligned} \tag{A42}$$

Again, $D^{(0)} = 0$ has been used for the second form and $\mathrm{sign}(x) = 1$ when $x > 0$ and -1 when $x < 0$.

Now we further simplify equation (A41) considering the two limiting cases corresponding to the electron and proton kinetic scales, respectively. Let us first consider the electron kinetic scale. By following the same steps as the $k_\parallel \neq 0$ case, the cold plasma dispersion relation and the derivative $\partial D_\perp^{(0)}/\partial \omega_r$ can respectively be simplified to

$$\frac{k^2c^2}{\omega_r^2} \approx \frac{c^2}{v_A^2} \frac{\omega_{\mathrm{lh}}^2}{\omega_{\mathrm{lh}}^2 - \omega_r^2 \left(1 + \frac{m_p}{m_e} \frac{v_A^2}{c^2}\right)} \approx \frac{c^2}{v_A^2} \frac{\omega_{\mathrm{lh}}^2}{\omega_{\mathrm{lh}}^2 - \omega_r^2} \text{ and} \tag{A43}$$

$$\frac{\partial D_\perp^{(0)}}{\partial \omega_r} \approx -2\frac{m_e}{m_p} \frac{c^4}{v_A^4} \frac{\omega_{\mathrm{lh}}^4}{\omega_r^3 \omega_{\mathrm{lh}}^2 - \omega_r^5 \left(1 + \frac{m_p}{m_e} \frac{v_A^2}{c^2}\right)} \approx -2\frac{m_e}{m_p} \frac{c^4}{v_A^4} \frac{\omega_{\mathrm{lh}}^4}{\omega_r^3 \omega_{\mathrm{lh}}^2 - \omega_r^5}, \tag{A44}$$

where $(m_e/m_p)(c/v_A)^2 \gg 1$ has been used for the final forms. The final growth rate formula becomes much simpler:

$$\frac{\gamma_l^2}{\omega_{\mathrm{lh}}^2} \approx \pi \frac{n_\sigma}{n_0} \frac{\omega_{r,l}^2}{\omega_{\mathrm{lh}}^2} \int_0^\infty \frac{\omega_{r,l}^2}{k^2} J_l^2 \frac{\partial H_\sigma}{\partial v_\perp} \mathrm{d}v_\perp. \tag{A45}$$

Note that equations (A43) and (A45) are consistent respectively with equations (2) and (3) derived by *Gul'elmi et al.* [1975] (apart from the factor π in γ_l which seems necessary and might be due to the different ways to normalize H_σ in the two studies). Same as equation (A28), $\gamma_l/\omega_{\mathrm{lh}}$ is also independent of m_p/m_e and c/v_A for fixed $\omega_r/\omega_{\mathrm{lh}}$.

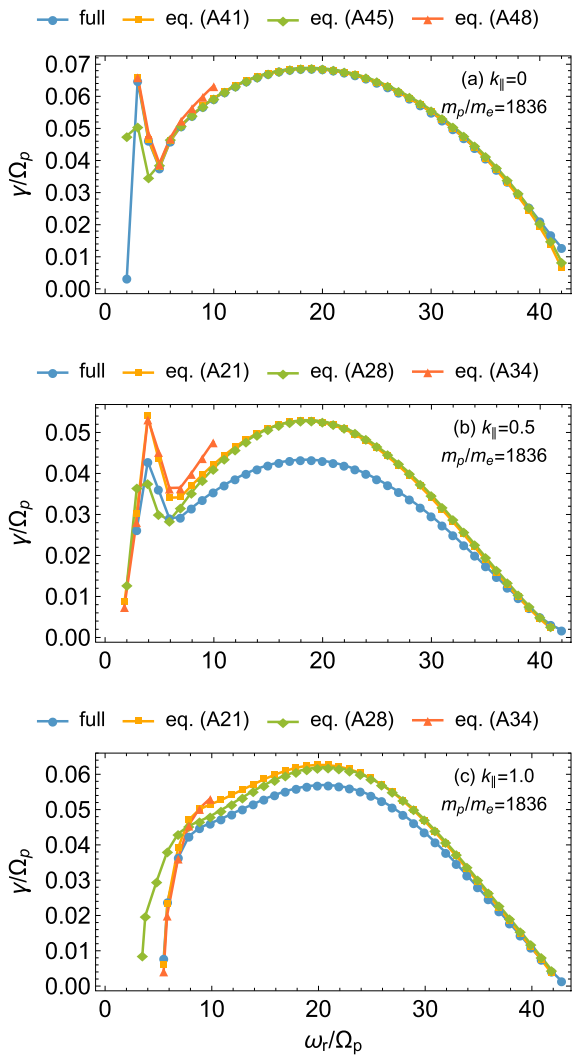

Figure A1. Comparison of the growth rates obtained from the approximate growth rate formulae (with the equation numbers labeled) with the full linear theory results (blue) for the ring model with $v_r/v_A = 2$ and $m_p/m_e = 1836$. (a–c) The $k_\parallel \lambda_p = 0$, 0.5, and 1 slices, respectively. Only the local maximum growth rates of the individual harmonic modes are shown.

Let us now consider the second limiting case, the proton kinetic scale. Again, following the same steps, the cold plasma dispersion relation and the derivative $\partial D_\perp^{(0)}/\partial\omega_r$ respectively read

$$kv_A \approx \omega_r \text{ and} \tag{A46}$$

$$\frac{\partial D_\perp^{(0)}}{\partial \omega_r} \approx -\frac{2}{\omega_r}\frac{c^4}{v_A^4}\frac{\Omega_p^2}{\omega_r^2 - \Omega_p^2}, \tag{A47}$$

and the growth rate is given by

$$\frac{\gamma_l^2}{\Omega_p^2} \approx \pi \frac{n_\sigma}{n_0}\int_0^\infty \left[\frac{\omega_{r,l}}{k}\frac{\omega_{r,l}}{\Omega_p}J_l - v_\perp J_l'\right]^2 \frac{\partial H_\sigma}{\partial v_\perp} dv_\perp. \tag{A48}$$

A3. Validation

Figure A1a compares the growth rates obtained from equations (A41), (A45), and (A48) with the full linear theory results for the ring model with $v_r/v_A = 2$, $m_p/m_e = 1836$ and $k_\parallel = 0$, showing rather excellent

agreement. Clearly, the growth rates valid for the electron kinetic scale (from equation (A45)) show good agreement in a wide frequency range ($\omega_r \gtrsim 5\Omega_p$), while the growth rates valid for the proton kinetic scale (from equation (A48)) show good agreement only at $\omega_r \lesssim 7\Omega_p$. Therefore, the further simplifications made to obtain equations (A45) and (A48) from equation (A41) are justified.

Figures A1b and A1c, corresponding to $k_\parallel \lambda_p = 0.5$ and 1, respectively, compare the maximum growth rates of the individual harmonics obtained from equations (A21), (A28), and (A34) with the full linear theory results for the ring model with $v_r/v_A = 2$, $m_p/m_e = 1836$. The overestimate from the approximate formulae derived is quite substantial for small $k_\parallel$ but is gradually reduced for large $k_\parallel$. This is rather puzzling, considering that the similar comparison in *Chen* [2015, Figure 2] showed better consistency. Without further investigation, we speculate that the growth rate may be too large, the cold plasma dispersion relation may be inaccurate, or the underlying energetic velocity distribution may somehow affect the results. We noticed though that the approximate formulae can produce the growth rate pattern (where the peaks and valleys occur) consistent with the full linear theory results (not shown). Nevertheless, as for the $k_\parallel = 0$ case, the growth rates valid for the electron and proton kinetic scales show good agreement with the growth rates obtained from equation (A21) in their respective frequency limits, indicating again that the further simplifications made to obtain equations (A28) and (A34) from equation (A21) are justified.

Acknowledgments
Data supporting the figures presented are available upon request from the corresponding author. The work at Auburn University was supported by NSF grant 1303623. Authors thank S. Peter Gary for helpful suggestions.

References

Arfken, G. B. (1985), *Mathematical Methods for Physicists*, 3rd ed., Academic Press, Orlando, Fla.

Boardsen, S. A., D. L. Gallagher, D. A. Gurnett, W. K. Peterson, and J. L. Green (1992), Funnel-shaped, low-frequency equatorial waves, *J. Geophys. Res.*, *97*(A10), 14,967–14,976, doi:10.1029/92JA00827.

Boardsen, S. A., et al. (2016), Survey of the frequency dependent latitudinal distribution of the fast magnetosonic wave mode from Van Allen Probes Electric and Magnetic Field Instrument and Integrated Science waveform receiver plasma wave analysis, *J. Geophys. Res. Space Physics*, *121*, 2902–2921, doi:10.1002/2015JA021844.

Chen, L. (2015), Wave normal angle and frequency characteristics of magnetosonic wave linear instability, *Geophys. Res. Lett.*, *42*, 4709–4715, doi:10.1002/2015GL064237.

Chen, L., and R. M. Thorne (2012), Perpendicular propagation of magnetosonic waves, *Geophys. Res. Lett.*, *39*, L14102, doi:10.1029/2012GL052485.

Chen, L., R. M. Thorne, V. K. Jordanova, and R. B. Horne (2010a), Global simulation of magnetosonic wave instability in the storm time magnetosphere, *J. Geophys. Res.*, *115*, A11222, doi:10.1029/2010JA015707.

Chen, L., R. M. Thorne, V. K. Jordanova, C.-P. Wang, M. Gkioulidou, L. Lyons, and R. B. Horne (2010b), Global simulation of EMIC wave excitation during the 21 April 2001 storm from coupled RCM-RAM-HOTRAY modeling, *J. Geophys. Res.*, *115*, A07209, doi:10.1029/2009JA015075.

Chen, L., R. M. Thorne, Y. Shprits, and B. Ni (2013), An improved dispersion relation for parallel propagating electromagnetic waves in warm plasmas: Application to electron scattering, *J. Geophys. Res. Space Physics*, *118*(5), 2185–2195, doi:10.1002/jgra.50260.

Chen, L., J. Sun, Q. Lu, X. Gao, Z. Xia, and Z. Zhima (2016), Generation of magnetosonic waves over a continuous spectrum, *J. Geophys. Res. Space Physics*, *121*, 1137–1147, doi:10.1002/2015JA022089.

Curtis, S., and C. Wu (1979), Gyroharmonic emissions induced by energetic ions in the equatorial plasmasphere, *J. Geophys. Res.*, *84*(A6), 2597–2607, doi:10.1029/JA084iA06p02597.

Gary, S. P., K. Liu, D. Winske, and R. E. Denton (2010), Ion Bernstein instability in the terrestrial magnetosphere: Linear dispersion theory, *J. Geophys. Res. Space Physics*, *115*, A12209, doi:10.1029/2010JA015965.

Gul'elmi, A., B. Klaine, and A. Potapov (1975), Excitation of magnetosonic waves with discrete spectrum in the equatorial vicinity of the plasmapause, *Planet. Space Sci.*, *23*(2), 279–286, doi:10.1016/0032-0633(75)90133-6.

Horne, R. B., G. V. Wheeler, and H. S. C. K. Alleyne (2000), Proton and electron heating by radially propagating fast magnetosonic waves, *J. Geophys. Res.*, *105*(A12), 27,597–27,610, doi:10.1029/2000JA000018.

Hrbáčková, Z., O. Santolík, F. Němec, E. Macúšová, and N. Cornilleau-Wehrlin (2015), Systematic analysis of occurrence of equatorial noise emissions using 10 years of data from the Cluster mission, *J. Geophys. Res. Space Physics*, *120*(2), 1007–1021, doi:10.1002/2014JA020268.

Kasahara, Y., H. Kenmochi, and I. Kimura (1994), Propagation characteristics of the ELF emissions observed by the satellite Akebono in the magnetic equatorial region, *Radio Sci.*, *29*(4), 751–767, doi:10.1029/94RS00445.

Kennel, C. (1966), Low-frequency whistler mode, *Phys. Fluids A*, *9*(11), 2190–2202, doi:10.1063/1.1761588.

Liu, K., S. P. Gary, and D. Winske (2011), Excitation of magnetosonic waves in the terrestrial magnetosphere: Particle-in-cell simulations, *J. Geophys. Res.*, *116*, A07212, doi:10.1029/2010JA016372.

Ma, Q., W. Li, R. M. Thorne, J. Bortnik, C. A. Kletzing, W. S. Kurth, and G. B. Hospodarsky (2016), Electron scattering by magnetosonic waves in the inner magnetosphere, *J. Geophys. Res. Space Physics*, *121*, 274–285, doi:10.1002/2015JA021992.

Mace, R. L. (2004), Generalized electron Bernstein modes in a plasma with a kappa velocity distribution, *Phys. Plasma*, *11*, 507–522, doi:10.1063/1.1635824.

Mace, R. L., and M. A. Hellberg (2009), A new formulation and simplified derivation of the dispersion function for a plasma with a kappa velocity distribution, *Phys. Plasma*, *16*(7), 072113, doi:10.1063/1.3179807.

Mace, R. L., R. D. Sydora, and I. Silin (2011), Effects of superthermal ring current ion tails on the electromagnetic ion cyclotron instability in multi-ion magnetospheric plasmas, *J. Geophys. Res.*, *116*, A05206, doi:10.1029/2010JA016393.

McClements, K. G., and R. O. Dendy (1993), Ion cyclotron harmonic wave generation by ring protons in space plasmas, *J. Geophys. Res.*, *98*(A7), 11,689–11,700, doi:10.1029/93JA00158.

McClements, K. G., R. O. Dendy, and C. N. Lashmore-Davies (1994), A model for the generation of obliquely propagating ULF waves near the magnetic equator, *J. Geophys. Res.*, *99*(A12), 23,685–23,693, doi:10.1029/94JA01979.

Meredith, N. P., R. B. Horne, and R. R. Anderson (2008), Survey of magnetosonic waves and proton ring distributions in the Earth's inner magnetosphere, *J. Geophys. Res.*, *113*, A06213, doi:10.1029/2007JA012975.

Min, K., and K. Liu (2015a), Fast magnetosonic waves driven by shell velocity distributions, *J. Geophys. Res. Space Physics*, *120*, 2739–2753, doi:10.1002/2015JA021041.

Min, K., and K. Liu (2015b), Regime transition of ion Bernstein instability driven by ion shell velocity distributions, *J. Geophys. Res. Space Physics*, *120*, 8448–8454, doi:10.1002/2015JA021514.

Min, K., and K. Liu (2016a), Understanding the growth rate patterns of ion Bernstein instabilities driven by ring-like proton velocity distributions, *J. Geophys. Res. Space Physics*, *121*, 3036–3049, doi:10.1002/2016JA022524.

Min, K., and K. Liu (2016b), Proton velocity ring-driven instabilities in the inner magnetosphere: Linear theory and particle-in-cell simulations, *J. Geophys. Res. Space Physics*, *121*, 475–491, doi:10.1002/2015JA022042.

Min, K., K. Liu, and S. P. Gary (2016), Scalings of Alfvén-cyclotron and ion Bernstein instabilities on temperature anisotropy of a ring-like velocity distribution in the inner magnetosphere, *J. Geophys. Res. Space Physics*, *121*, 2185–2193, doi:10.1002/2015JA022134.

Němec, F., O. Santolík, J. S. Pickett, Z. Hrbáčková, and N. Cornilleau-Wehrlin (2013), Azimuthal directions of equatorial noise propagation determined using 10 years of data from the Cluster spacecraft, *J. Geophys. Res. Space Physics*, *118*, 7160–7169, doi:10.1002/2013JA019373.

Němec, F., O. Santolík, K. Gereová, and E. Macúšová (2005), Initial results of a survey of equatorial noise emissions observed by the Cluster spacecraft, *Planet. Space Sci.*, *53*(1–3), 291–298, doi:10.1016/j.pss.2004.09.055.

Němec, F., O. Santolík, K. Gereová, E. Macúšová, and H. Laakso (2006), Equatorial noise: Statistical study of its localization and the derived number density, *Adv. Space Res.*, *37*(3), 610–616, doi:10.1016/j.asr.2005.03.025.

Perraut, S., A. Roux, P. Robert, R. Gendrin, J.-A. Sauvaud, J.-M. Bosqued, G. Kremser, and A. Korth (1982), A systematic study of ULF waves above f_{H+} from GEOS 1 and 2 measurements and their relationships with proton ring distributions, *J. Geophys. Res. Space Physics*, *87*(A8), 6219–6236, doi:10.1029/JA087iA08p06219.

Posch, J. L., M. J. Engebretson, C. N. Olson, S. A. Thaller, A. W. Breneman, J. R. Wygant, S. A. Boardsen, C. A. Kletzing, C. W. Smith, and G. D. Reeves (2015), Low-harmonic magnetosonic waves observed by the Van Allen Probes, *J. Geophys. Res. Space Physics*, *120*, 6230–6257, doi:10.1002/2015JA021179.

Qureshi, M. N. S., W. Nasir, W. Masood, P. H. Yoon, H. A. Shah, and S. J. Schwartz (2014), Terrestrial lion roars and non-Maxwellian distribution, *J. Geophys. Res. Space Physics*, *119*, 10,059–10,067, doi:10.1002/2014JA020476.

Russell, C. T., R. E. Holzer, and E. J. Smith (1970), OGO 3 observations of ELF noise in the magnetosphere: 2. The nature of the equatorial noise, *J. Geophys. Res.*, *75*(4), 755–768, doi:10.1029/JA075i004p00755.

Santolík, O., J. S. Pickett, D. A. Gurnett, M. Maksimovic, and N. Cornilleau-Wehrlin (2002), Spatiotemporal variability and propagation of equatorial noise observed by Cluster, *J. Geophys. Res.*, *107*, 1495, doi:10.1029/2001JA009159.

Shaaban, S. M., M. Lazar, S. Poedts, and A. Elhanbaly (2016), The interplay of the solar wind proton core and halo populations: EMIC instability, *J. Geophys. Res. Space Physics*, *121*, doi:10.1002/2016JA022587.

Stix, T. H. (1992), *Waves in Plasmas, Am. Inst. Phys.*, Springer, New York.

Sugiyama, H., S. Singh, Y. Omura, M. Shoji, D. Nunn, and D. Summers (2015), Electromagnetic ion cyclotron waves in the Earth's magnetosphere with a kappa-Maxwellian particle distribution, *J. Geophys. Res. Space Physics*, *120*, 8426–8439, doi:10.1002/2015JA021346.

Sun, J., X. Gao, L. Chen, Q. Lu, X. Tao, and S. Wang (2016a), A parametric study for the generation of ion Bernstein modes from a discrete spectrum to a continuous one in the inner magnetosphere. I. Linear theory, *Phys. Plasma*, *2*, 022901, doi:10.1063/1.4941283.

Sun, J., X. Gao, Q. Lu, L. Chen, X. Tao, and S. Wang (2016b), A parametric study for the generation of ion Bernstein modes from a discrete spectrum to a continuous one in the inner magnetosphere. II. Particle-in-cell simulations, *Phys. Plasma*, *23*(2), 022902, doi:10.1063/1.4941284.

Thomsen, M. F., M. H. Denton, V. K. Jordanova, L. Chen, and R. M. Thorne (2011), Free energy to drive equatorial magnetosonic wave instability at geosynchronous orbit, *J. Geophys. Res. Space Physics*, *116*, A08220, doi:10.1029/2011JA016644.

Umeda, T., S. Matsukiyo, T. Amano, and Y. Miyoshi (2012), A numerical electromagnetic linear dispersion relation for Maxwellian ring-beam velocity distributions, *Phys. Plasma*, *19*(7), 072107, doi:10.1063/1.4736848.

Viñas, A. F., R. L. Mace, and R. F. Benson (2005), Dispersion characteristics for plasma resonances of Maxwellian and Kappa distribution plasmas and their comparisons to the IMAGE/RPI observations, *J. Geophys. Res. Space Physics*, *110*, A06202, doi:10.1029/2004JA010967.

Walker, S. N., M. A. Balikhin, D. R. Shklyar, K. H. Yearby, P. Canu, C. M. Carr, and I. Dandouras (2015), Experimental determination of the dispersion relation of magnetosonic waves, *J. Geophys. Res. Space Physics*, *120*, 9632–9650, doi:10.1002/2015JA021746.

Xiao, F., Q. Zhou, H. He, H. Zheng, and S. Wang (2007), Electromagnetic ion cyclotron waves instability threshold condition of suprathermal protons by kappa distribution, *J. Geophys. Res.*, *112*, A07219, doi:10.1029/2006JA012050.

Xiao, F., C. Shen, Y. Wang, H. Zheng, and S. Wang (2008), Energetic electron distributions fitted with a relativistic kappa-type function at geosynchronous orbit, *J. Geophys. Res.*, *113*, A05203, doi:10.1029/2007JA012903.

Xiao, F., Q. Zhou, Z. He, and L. Tang (2012), Three-dimensional ray tracing of fast magnetosonic waves, *J. Geophys. Res.*, *117*, A06208, doi:10.1029/2012JA017589.

Xiao, F., C. Yang, Z. Su, Q. Zhou, Z. He, Y. He, D. N. Baker, H. E. Spence, H. O. Funsten, and J. B. Blake (2015), Wave-driven butterfly distribution of Van Allen belt relativistic electrons, *Nat. Commun.*, *6*, 8590, doi:10.1038/ncomms9590.